

A Census of Na D-traced neutral ISM and outflows at $0.6 < z < 4$

YANG SUN ¹, ZHIYUAN JI ¹, FRANCESCO D'EUGENIO ^{2,3}, YONGDA ZHU ¹, GEORGE H. RIEKE ¹,
WILLIAM M. BAKER ⁴, ANDREW J. BUNKER ⁵, STEFANO CARNIANI ⁶, JAKOB M. HELTON ⁷, MICHELE PERNA ⁸,
PABLO G. PÉREZ-GONZÁLEZ ⁸, PIERLUIGI RINALDI ⁹, HANNAH ÜBLER ¹⁰ AND CHRISTOPHER N. A. WILLMER ¹

¹Steward Observatory, University of Arizona, 933 North Cherry Avenue, Tucson, AZ 85719, USA

²Kavli Institute for Cosmology, University of Cambridge, Madingley Road, Cambridge, CB3 0HA, UK

³Cavendish Laboratory, University of Cambridge, 19 JJ Thomson Avenue, Cambridge, CB3 0HE, UK

⁴DARK, Niels Bohr Institute, University of Copenhagen, Jagtvej 155A, DK-2200 Copenhagen, Denmark

⁵Department of Physics, University of Oxford, Denys Wilkinson Building, Keble Road, Oxford OX1 3RH, UK

⁶Scuola Normale Superiore, Piazza dei Cavalieri 7, I-56126 Pisa, Italy

⁷Department of Astronomy & Astrophysics, The Pennsylvania State University, University Park, PA 16802, USA

⁸Centro de Astrobiología (CAB), CSIC-INTA, Cra. de Ajalvir Km. 4, 28850- Torrejón de Ardoz, Madrid, Spain

⁹Space Telescope Science Institute, 3700 San Martin Drive, Baltimore, Maryland 21218, USA

¹⁰Max-Planck-Institut für extraterrestrische Physik (MPE), Gießenbachstraße 1, 85748 Garching, Germany

ABSTRACT

We present a statistical census of the Na D-traced neutral interstellar medium (ISM) and outflows in 309 galaxies at $0.6 < z < 4$ using JWST/NIRSpec medium-resolution grating spectroscopy from the SMILES, JADES, Blue Jay, and Aurora surveys. After subtracting the stellar continuum, we model the Na D $\lambda\lambda 5890, 5896 \text{ \AA}$ and detect neutral ISM absorption in 76 galaxies. Of the Na D-traced ISM detections, 85% are found in massive galaxies ($\log(M_*/M_\odot) > 10$), and only 15% in lower-mass systems. In the massive regime, ISM absorption is seen in both star-forming and quiescent galaxies, whereas in lower-mass systems it is observed only in star-forming galaxies. In massive quiescent galaxies, Na D detectability appears linked to star formation history: it is preferentially detected in older systems with larger 4000 \AA breaks, as well as younger, rapidly quenching galaxies with strong Balmer absorption $H\delta_A$. We identify Na D outflows in 26 galaxies, revealing a possible dichotomy in their driving mechanisms between star-forming and quiescent galaxies. In star-forming galaxies, outflow properties correlate with star-formation properties, consistent with a star-formation-driven origin. In quiescent galaxies, however, outflows are not associated with residual star formation and often require more energy than such star formation can provide. Together with the high AGN fraction among outflow-detected quiescent galaxies, this suggests that AGN dominate Na D-traced neutral outflows in cosmic noon quiescent systems. We further identify five quiescent galaxies with possible AGN fossil outflows, suggesting that AGN-driven outflows can persist beyond the active accretion phase and may help maintain quiescence.

Keywords: Galactic Winds (572), Galaxy Evolution (594), Star Formation (1569), Galaxy Quenching (2040)

1. INTRODUCTION

Observations in both the local Universe and at high redshift have revealed a clear bimodality in galaxy color, morphology, and star formation activity, with galaxies broadly divided into star-forming and quiescent populations (e.g., I. Strateva et al. 2001; G. Kauffmann et al.

2003; J. Brinchmann et al. 2004; K. G. Noeske et al. 2007; J. S. Speagle et al. 2014; S. Tacchella et al. 2016; Z. Ji & M. Giavalisco 2023). Understanding quenching, i.e. the processes that causes star formation to cease and transforms galaxies from star-forming systems into quiescent ones, remains a central problem in galaxy evolution.

Feedback is widely thought to be essential for quenching (e.g., D. Kereš et al. 2009; P. F. Hopkins et al. 2014; R. S. Somerville et al. 2015; T. Naab & J. P. Ostriker

2017; J. Silk & M. J. Rees 1998; P. F. Hopkins et al. 2008; A. Man & S. Belli 2018), but its detailed physics remain poorly understood. By injecting energy and momentum into galaxies, feedback shapes the gas within and around them, but this is observationally difficult to characterize because galaxies host multiphase gas spanning a wide range of temperatures and densities. To understand how feedback drives galaxy quenching, we therefore need a census of outflows across gas phases and galaxy evolutionary stages. So far, the ionized phase has been studied most extensively, thanks to bright emission lines such as [O III] and H α (e.g., J.-H. Woo et al. 2016; A. Concas et al. 2017; N. M. Förster Schreiber et al. 2019). In contrast, cooler gas, especially the neutral and molecular phases ($T \lesssim 10^4$ K), remains much less constrained, despite being more directly tied to star-forming fuel. This is particularly true in quiescent galaxies, where emission lines are often faint or even entirely absent. Observations of these phases remain limited to small samples, despite their importance for tracing gas removal and redistribution (S. Veilleux et al. 2020; K. D. French et al. 2015; J. Spilker et al. 2018; C. C. Williams et al. 2021; R. Bezanson et al. 2022, and references therein).

The Na D doublet is particularly powerful in this context because it probes the cool neutral gas phase that is otherwise difficult to access, especially in quiescent galaxies. It is a resonant transition of neutral sodium at rest-frame 5890 Å and 5896 Å, commonly observed in absorption against the stellar continuum and also capable of exhibiting resonant emission through scattering and re-emission in outflowing gas (e.g., J. X. Prochaska et al. 2011). Its absorption profile provides a sensitive probe of the column density and kinematics of neutral gas along the line of sight, thereby offering a direct way to connect feedback signatures to the cool ISM and its associated dust during galaxy evolution.

In the local Universe, Na D has been extensively studied as a tracer of the neutral ISM and its connection to feedback. Na D-traced ISM is commonly detected in star-forming and starburst galaxies (e.g., D. S. Rupke et al. 2005a; Y.-M. Chen et al. 2010; S. Cazzoli et al. 2016; A. Concas et al. 2019) and in AGN hosts (e.g., M. Sarzi et al. 2016; A. Fluetsch et al. 2021; M. Perna et al. 2019). It is also frequently detected in local post-starburst galaxies (PSBs) that were quenched within the past ~ 1 Gyr, and which in many cases show signatures of outflowing neutral gas (e.g., C. A. Tremonti et al. 2007; A. L. Coil et al. 2011; Y. Luo et al. 2022; D. Baron et al. 2022; Y. Sun et al. 2024). By contrast, Na D-traced ISM is rare in local quiescent galaxies that have remained quenched for longer periods (Y. Sun et al. 2024). These results suggest that substantial cool gas

reservoirs can persist into the quenching phase and are often kinematically disturbed, but that this gas is largely depleted in galaxies long after quenching.

At $z > 1$, Na D studies were long hampered by the wavelength coverage and sensitivity limits of pre-JWST facilities. Yet constraining the neutral ISM at cosmic noon is particularly important, because this is the epoch when star formation and black hole growth peak (P. Madau & M. Dickinson 2014) and galaxies transition rapidly across evolutionary stages (e.g., A. Muzzin et al. 2013). With the launch of JWST (J. P. Gardner et al. 2006), Na D-traced neutral ISM detections, especially outflows, have increasingly been reported in galaxies at cosmic noon and beyond, initially in individual systems (S. Belli et al. 2024; F. D’Eugenio et al. 2024a; P. G. Pérez-González et al. 2025; P.-F. Wu 2025; Y. Sun et al. 2026) and more recently in a few survey-level studies, though still with limited sample sizes (5–30 detections; R. L. Davies et al. 2024; E. Taylor et al. 2026; P. Zhu et al. 2026).

Even within these limited samples, Na D studies have already revealed several intriguing trends at cosmic noon. Na D outflows have been identified in quiescent galaxies with ongoing AGN activity (e.g., S. Belli et al. 2024; R. L. Davies et al. 2024; F. D’Eugenio et al. 2024a; P.-F. Wu 2025), but also in a few $z > 1$ quiescent galaxies without clear evidence for such activity (P. G. Pérez-González et al. 2025; Y. Sun et al. 2026; E. Taylor et al. 2026; P. Zhu et al. 2026). This suggests that the physical drivers of Na D-traced neutral outflows are not straightforward: in some cases they may be linked to ongoing AGN feedback, while in others they may reflect fossil AGN or other mechanisms. Taken together, these results imply that neutral outflows may arise in quenching systems under a range of physical conditions, underscoring the need for a statistical census of the neutral-phase ISM and outflows across galaxy evolutionary stages at cosmic noon to determine how common they are and what role they play in early massive-galaxy quenching.

To this end, we present a census of Na D-traced ISM and outflows at $0.6 < z < 4$ based on a compilation of JWST/NIRSpec medium-grating ($R \sim 1000$) spectroscopy from Cycles 1–3 programs, including SMILES (G. H. Rieke et al. 2024; S. Alberts et al. 2024), JADES (A. J. Bunker et al. 2024; D. J. Eisenstein et al. 2026, 2023), Blue Jay (S. Belli et al. 2025), and Aurora (A. E. Shapley et al. 2025). This yields the largest dataset to date for this purpose, comprising 309 galaxies with spectra of sufficient quality for detailed Na D analysis and spanning evolutionary stages from star-forming to quiescent. Using this sample, we measure the incidence of

Na D-traced ISM absorption, the prevalence and kinematics of neutral outflows, and their dependence on host-galaxy star formation and AGN properties. This dataset provides a statistical view of the cool neutral phase across the quenching sequence at cosmic noon.

This paper is organized as follows: We present the data used in this study in Section 2, and the sample drawn from it in Section 3. We then describe the spectral analysis and the SED modelling in Section 4. The census results for Na D-traced ISM are in Section 5.1 and outflows in Section 5.2. We discuss their implications on the outflow driving mechanisms, multiphase natures, and correlation with different galaxy quenching pathways in Section 6. Finally, we summarize our work in Section 7. Throughout this paper, we assume a standard Λ CDM universe whose cosmological parameters are $H_0 = 70 \text{ km s}^{-1} \text{ Mpc}^{-1}$, $\Omega_\Lambda = 0.7$, and $\Omega_m = 0.3$.

2. DATA

We compiled JWST NIRSpec/Micro Shutter Assembly (MSA; P. Jakobsen et al. 2022; P. Ferruit et al. 2022) G140M and G235M medium-resolution grating ($R \sim 1000$) spectra from four surveys that have good coverage of cosmic noon galaxies: SMILES in GOODS-S/UDF, JADES in GOODS-S and -N, Blue Jay in COSMOS, and Aurora in COSMOS and GOODS-N. These setups cover the Na D feature for galaxies at $0.6 < z < 4$, enabling an analysis of neutral gas absorption across a broad range of redshift and galaxy types.

The spectroscopic data reductions adopted for each survey are listed in Table 1. We use spectra reduced with local background subtraction using the default DJA setup, namely three-nod subtraction for SMILES, JADES, and Aurora, and “A–B” subtraction for the two-shutter Blue Jay slitlets¹¹. Although this approach might lead to self-subtraction in extended galaxies, Appendix C shows that the effect is negligible for our Na D ISM profile modeling and scientific conclusions. In addition, because our $z \sim 2$ targets are often spatially extended, the MSA shutter usually does not cover the full galaxy. We therefore estimate slit-loss corrections by matching synthetic slit photometry to the full-galaxy NIRCам photometry. This procedure implicitly assumes spatially uniform line-to-continuum ratios and similar spatial distributions for nearby lines (e.g., [N II] and $H\alpha$), which may not always hold. To minimize potential systematics, we apply the slit-loss correction only when deriving quantities that require absolute

line luminosities, such as $H\alpha$ -based SFRs (Appendix B) and [O III]-based AGN luminosities (Section 5.2.3). For stellar-population fitting (Section 4.1), Na D profile measurements (Section 4.2), and line-ratio diagnostics including Balmer decrements (Section 4.1) and BPT diagrams (Section 5.1.4), we use the uncorrected spectra.

For photometry, we use the published catalogs in each survey field, also summarized in Table 1. We adopt all available HST/ACS and WFC3, and JWST/NIRCам measurements to sample the rest-frame optical-to-near-IR SEDs of the galaxies, enabling reliable constraints on their stellar properties.

3. THE SAMPLE

Our initial sample is drawn from the full set of galaxies with spectroscopy in the surveys listed in Table 1, where the total number of spectra in each field is also reported. We first restrict the redshift range to $0.6 < z < 4$, such that the Na D doublet is covered by either the G140M or G235M grating. Because detecting and modeling Na D absorption requires robust continuum measurements, we further refine the sample by requiring the average per-pixel continuum SNR adjacent to Na D, measured over rest-frame 5850–5870 Å and 5910–5930 Å, to satisfy $\text{SNR}_{\text{cont}} > 5$. This yields a spectral parent sample of 314 galaxies at $0.6 < z < 4$ (Table 1). After cross-matching with the photometric catalogs, two JADES galaxies and three Aurora galaxies are excluded from further analysis because of missing photometric counterparts or large photometric uncertainties.

Our final sample comprises 309 galaxies at $0.6 < z < 4$, all with NIRSpec $R \sim 1000$ spectra of sufficient quality for Na D modeling and with UV-to-NIR photometry for stellar-population inference. The sample includes 63 SMILES galaxies, 159 JADES galaxies, 56 Blue Jay galaxies, and 31 Aurora galaxies. The redshift and M_* -sSFR distributions of the parent sample are shown in Figures 1 and 2, respectively.

4. ANALYSIS

In this section, we describe the steps used to isolate the Na D absorption arising from the ISM in the observed spectra. Specifically, we (1) correct the Na D absorption for the contribution due to stars rather than the ISM (Section 4.1); (2) fit possible Na D line profiles and measure their strength (Section 4.2); and (3) evaluate whether these results indicate a detection at a significant level and if so, whether the detection is an inflow, outflow, or at the systemic velocity (Section 4.3). Then, in Section 4.4, we describe the SED modeling we use to determine the host galaxy properties, particularly their current levels of star formation and their star formation histories.

¹¹ Blue Jay spectra are observed with a two-shutter slitlet, so the DJA reduction is based on local background subtraction, i.e., “A–B” subtraction.

Table 1. Survey sample summary

Survey	Spectroscopy	Photometry	N_{initial}^a	N_{final}^b
SMILES	SMILES DR2 ^c	JADES DR5 ^d	166	63
JADES	JADES DR4 ^e	JADES DR5	4752	159
Blue Jay	DJA ^f	Blue Jay DR ^g	153	56
Aurora	DJA	JADES DR5 & DJA	97	31
Total			5168	309

NOTE—^aTotal number of published spectra of each survey; ^bFinal sample defined by requiring $0.6 < z < 4$, and $\text{SNR}_{\text{cont}} > 5$ in the continuum adjacent to Na D, measured over rest-frame 5850–5870 Å and 5910–5930 Å, and with available HST and JWST photometry measurements. ^cY. Zhu et al. (2026); ^dB. D. Johnson et al. (2026); B. E. Robertson et al. (2026); ^eE. Curtis-Lake et al. (2025); J. Scholtz et al. (2025); ^fDawn JWST Archive; K. E. Heintz et al. (2025); A. de Graaff et al. (2025); ^g<https://zenodo.org/records/13292819>

4.1. Stellar continuum and nebular emission modeling using pPXF

Both the stellar photosphere and the ISM can contribute to Na D spectral features; therefore, we model the stellar continuum of each galaxy spectrum over the wavelength range of 3500–7500 Å in the rest-frame using penalized pixel fitting (pPXF, M. Cappellari & E. Emsellem 2004; M. Cappellari 2017). We adopt the instrument line spread function from P. Jakobsen et al. (2022). Our pPXF setup is similar to F. D’Eugenio et al. (2024a). We build stellar templates using the Flexible Stellar Population Synthesis (FSPS; C. Conroy et al. 2009; C. Conroy & J. E. Gunn 2010) model built by M. Cappellari (2023), with the C3K stellar spectral library (M. Park et al. 2025), the MIST isochrones (J. Choi et al. 2016) and the Salpeter IMF (E. E. Salpeter 1955). The templates span a logarithmically spaced grid of ages and metallicities, covering the range of 1 Myr–15.85 Gyr with 0.1 dex sampling and $[Z/H]=-1.75-0.25$ with 0.25 dex sampling, respectively. The age of the input templates is required not to exceed the Universe age at the redshift of each galaxy.

In pPXF fitting, we also simultaneously fit the nebular emission lines, including Balmer lines, [O III] $\lambda\lambda 4959, 5007$, [O I] $\lambda 6300$, [N II] $\lambda\lambda 6548, 6584$, and [S II] $\lambda\lambda 6717, 6731$. A single Gaussian profile is assigned to each line, sharing the same velocity and velocity dispersion. The line velocity dispersions are limited within 300 km s^{-1} , and the velocity offset is restricted within $\pm 200 \text{ km s}^{-1}$ relative to the systemic redshift.

Finally, a multiplicative polynomial¹² is applied to avoid mismatches between galaxy spectra and stellar templates and ensure the accuracy of fitted kinematic

parameters. The Na D line is masked during fitting to avoid the influence of Na D ISM absorption on the stellar Na D absorption modeling.

The systemic redshift is determined by pPXF. Ideally, we aim to anchor the systemic redshift using stellar absorption features, as the Na D outflow we seek is defined by Na D ISM absorption that is blueshifted relative to background stellar light. However, in reality, most galaxies in our sample do not exhibit clear stellar absorption lines but rather strong emission lines. In this case, we measure the systemic redshift using the emission lines.

We measure emission line fluxes from the best-fit nebular components in the pPXF model. To estimate flux uncertainties, we perform 100 Monte Carlo realizations of the pPXF fitting. We then derive the dust attenuation (A_V) primarily from the Balmer decrement $H\alpha/H\beta$. We assume Case B recombination and $T_e = 10^4 \text{ K}$, and hence an intrinsic Balmer flux ratio $(H\alpha/H\beta)_0 = 2.86$. If the SNR of either $H\alpha$ or $H\beta$ is less than three, we instead adopt the SED-based A_V (SED modeling will be presented in Section 4.4)¹³. Finally, we use the D. Calzetti et al. (2000) reddening curve to dust-correct the line fluxes.

4.2. Na D excess profile modeling

After subtracting the stellar Na D contribution with pPXF, we model the residual Na D absorption from the ISM following Y. Sun et al. (2026):

$$F(\lambda) = F_* \times F_{\text{Na D, ISM}}, \quad (1)$$

where F_* is the pPXF stellar continuum and $F_{\text{Na D, ISM}}$ is described with the standard partial-covering formal-

¹² In most cases, we adopt a fourth-degree polynomial. However, for a small subset of galaxies in which visual inspection reveals a significant mismatch between the G140M and G235M continuum levels, likely due to contamination, we increase the polynomial degree to 12.

¹³ In fact, about 60% of A_V of our parent galaxy sample is measured through the Balmer Decrement, and the other 40% is derived from SED fitting. As a sanity check, we compare the two independent A_V measurements for galaxies with both available and find that they are broadly consistent.

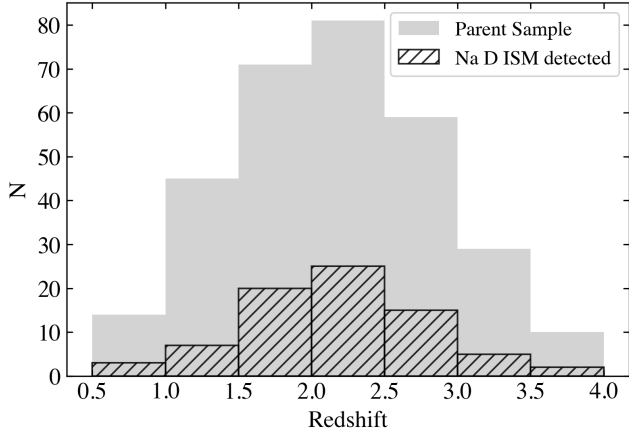


Figure 1. Redshift distributions of the final sample of 309 galaxies and the subsample of 72 galaxies with detected Na D ISM absorption.

ism of D. S. Rupke et al. (2005b):

$$F_{\text{Na D, ISM}}(\lambda) = 1 - C_f + C_f e^{(-\tau_b(\lambda) - \tau_r(\lambda))}, \quad (2)$$

with covering fraction C_f and Gaussian optical-depth profiles for the blue (τ_b) and red (τ_r) doublet components, assuming $\tau_b/\tau_r = 2$. The model-free parameters, therefore, are the line centroid λ_0 , optical depth τ_b , Doppler width b after considering the instrumental broadening, and covering fraction C_f .

In addition, with our spectral resolution of $R \sim 1000$, the He I $\lambda 5877$ emission would be partially blended with Na D. Therefore, we add an additional Gaussian component to model He I $\lambda 5877$, for which the line width and velocity are fixed to that of other lines determined by pPXF (Section 4.1). We apply the Bayesian information criterion (BIC) method to assess whether He I $\lambda 5877$ is present. If the difference of BIC between the model without and with He I emission exceeds 10 ($\Delta\text{BIC} = \text{BIC}_{\text{w/HeI}} - \text{BIC}_{\text{w/oHeI}} > 10$), we consider He I to be detected. To this end, for the model with He I, one more parameter, F_{HeI} , is added.

Finally, we run Markov Chain Monte Carlo (MCMC) to fit the model with `emcee` to estimate the parameter uncertainties and account for the well-known degeneracy between optical depth and covering fraction in blended Na D absorption (D. S. Rupke et al. 2005b; R. L. Davies et al. 2024). Full details of the model setup, fitting procedure, and validation are given in Y. Sun et al. (2026).

4.3. Na D ISM detection and flow classification

To quantify the amount of Na D ISM absorption and evaluate the confidence of the Na D ISM detection, we measure the equivalent width ($\text{EW}_{\text{NaD,ISM}}$, where positive means absorption and negative means emis-

sion), and the SNR of the Na D ISM absorption minimum relative to the mean noise of the adjacent continuum ($\text{SNR}_{\text{NaD,ISM}}$). We define the “Na D ISM absorption detected” galaxy sample by requiring $\text{EW}_{\text{NaD,ISM}} - \sigma(\text{EW}_{\text{NaD,ISM}}) > 0$ and $\text{SNR}_{\text{NaD,ISM}} > 1.5$, together with visual inspection.¹⁴

After this procedure, 76 galaxies have a Na D ISM absorption detection, including 13 from SMILES, 36 from JADES, 21 from Blue Jay, and 6 from Aurora. We note that, R. L. Davies et al. (2024) reported 30 Na D absorption detections, while we only detected 21. We find three of them does meet our requirement of Na D-surrounding continuum detection $\text{SNR}_{\text{cont}} > 5$, and another six do not meet the Na D absorption significance requirements. Some of this discrepancy might also be due to differences in data reduction between R. L. Davies et al. (2024) and DJA.

Among the 76 galaxies with Na D ISM absorption, we find that four are broad-line (BL) AGN reported by previous works (I. Juodžbalis et al. 2026; L. Bugiani et al. 2025). Given that, for bright BL AGN, the spectroscopic stellar population synthesis and Na D profile modeling can become unreliable when the spectrum is dominated by strong AGN power-law emission and broad-line features, we exclude them from the following analysis but only show their locations in Figure 2.

Depending on the geometry, it is also possible to see Na D emission rather than absorption, when absorbed photons are re-emitted along the line of sight due to resonant scattering (J. X. Prochaska et al. 2011). We detect Na D emission in one galaxy (SMILES-196290), which is identified as a BL AGN (Y. Sun et al. 2025) with strong extended ionized emission (Y. Zhu et al. 2025). Therefore, the Na D emission might be attributed to the Na D-traced ISM ionized by the strong AGN radiation, which thus also indicates the presence of Na D ISM in SMILES-196290. However, discussion of the Na D emission is beyond the scope of this work; therefore, in the following analysis, we focus only on galaxies with Na D ISM absorption.

To better quantify the measurement uncertainty of the Na D ISM profile of the 72 remaining Na D-ISM detected galaxies (five BL AGN are removed), we per-

¹⁴ After visual inspection, we find that the cut at $\text{SNR}_{\text{NaD,ISM}} > 1.5$ and $\text{EW}_{\text{NaD,ISM}} 1\sigma$ significance yields 90% solid Na D ISM detections. The remaining 10% contaminants are due to either poor pPXF fits resulting in a contaminated continuum, or the noise when Na D is close to the edge of filter. Furthermore, our visual inspection does not recover any convincing Na D detections among galaxies with $\text{SNR}_{\text{NaD,ISM}} < 1.5$ and/or $\text{EW}_{\text{NaD,ISM}} < 1\sigma$ detection that were initially classified as non-detections.

form a Monte Carlo evaluation, i.e., generating 100 mock spectra based on the observed flux errors and rerun the pPXF and Na D ISM profile fitting described in Sections 4.1 and 4.2. The best-fit Na D profile parameters and their 1σ upper and lower errors are derived from the combined 100 MCMC posterior distributions. From this process, we are able to classify the flow direction of Na D ISM in those galaxies as: outflow if the 68th confidence interval of ΔV is negative; inflow if the 68th confidence interval of ΔV is positive; systemic, for all other cases. By this definition, we identify 26 Na D outflows, 10 inflows, and 36 systemic cases. We notice that three outflows identified by R. L. Davies et al. (2024) (BJ-10565, 11494, and 10021) are classified as systemic ISM based on our analysis. Such a kinematic discrepancy could be due to moderate spectral resolution ($R \sim 1000$) and slightly different data reduction procedures. Therefore, we do not include those three galaxies in our Na D outflow census in Section 5.2. We confirm that our scientific conclusion will not change even if we include them in the analysis.

Finally, the best-fit Na D ISM profile of all the 72 Na D ISM absorption-detected galaxies is displayed in Appendix A. The derived Na D profile parameters, as well as host galaxy properties, for the Na D inflows, systemic ISM, and outflows are shown in Appendix Table A2, A3 and A1, respectively.

4.4. SED modeling

We fit the galaxy photometry with the Prospector code (B. D. Johnson et al. 2021). Our assumptions for the SEDs, including parameter priors, are similar to those used in Z. Ji et al. (2024a). In brief, we fix the redshift to the spectroscopic redshift modeled by pPXF (Section 4.1). We use the Kroupa stellar IMF (P. Kroupa 2001), and adopt the FSPS stellar synthesis code (C. Conroy et al. 2009; C. Conroy & J. E. Gunn 2010) with the stellar isochrone libraries MIST (J. Choi et al. 2016) and the MILES stellar spectral libraries (P. Sánchez-Blázquez et al. 2006; J. Falcón-Barroso et al. 2011). We use the Madau intergalactic material (IGM) transmission model (P. Madau 1995). We include the nebular emission model from N. Byler et al. (2017). We leave the stellar metallicity (Z_*), the gas metallicity (Z_{gas}), and the ionization parameter (U) as free parameters. We use a two-component dust attenuation model, where the attenuations toward nebular emission and young (< 10 Myr) stellar populations are modeled by a power law, and those towards old (> 10 Myr) stellar populations are treated following the parameterization of S. Noll et al. (2009), a modified D. Calzetti et al. (2000) law with the 2175Å dust feature.

We also include active AGN dust torus templates from M. Nenkova et al. (2008a) and M. Nenkova et al. (2008b) to account for AGN contributions to the galaxy SED.

Our default model adopts a nonparametric star formation history (SFH) with nine lookback time bins and the bursty continuity prior (J. Leja et al. 2017; S. Tacchella et al. 2022). The first two bins are fixed to be 0-30 and 30-100 Myr to capture recent star formation activity. The final bin spans $0.85t_H - t_H$ where t_H is the Hubble time at the representative redshift. The remaining six bins are evenly spaced in logarithmic time between 100 Myr and $0.85t_H$.

The reliability of our SED modeling is supported by a sanity check in which we compare the SFRs over the most recent 30 Myr inferred from photometry-based SED fitting with slit-loss- and dust-corrected $H\alpha$ -based SFRs (see Appendix B). The quiescent galaxies are identified as having a position 0.5 dex below the main sequence as inferred from their SED-based SFR (see details in Section 5.1). We cross-match them with the sub-millimeter source catalogs, including ASPECS-LP (M. Aravena et al. 2020) and A3GOODS (S. Adscheid et al. 2024) in GOODS-S, Super GOODS (L. L. Cowie et al. 2017) in GOODS-N, and A3COSMOS (D. Liu et al. 2019) in COSMOS, to see if any of them may have significant dust-obscured star formation. While ~ 10 quiescent galaxies have sub-millimeter detections, we find, in most of the cases, those galaxies have AGNs; for the rest without AGNs, the SFRs derived from SED modeling including sub-millimeter data are not significantly larger than our estimate with only UV-to-NIR photometry and in no case do they shift these galaxies back onto the main sequence. Only one galaxy, SMILES-207739 at $z=1.04$, shows a notable difference: our SED fitting based on UV-to-NIR data alone returns an almost zero SFR, whereas including the sub-millimeter data increases the inferred SFR to $18 M_\odot \text{ yr}^{-1}$ (M. Aravena et al. 2020). However, even with this higher SFR, the galaxy still lies below the main sequence by about 0.5 dex. Overall, our UV-to-NIR SED modeling yields robust SFR estimates for the population analysis. Therefore, we adopt the SED-inferred SFR over the past 30 Myr as the fiducial SFR in the following analysis.

5. RESULTS

5.1. The incidence of Na D ISM at $0.6 < z < 4$

In this section, we investigate the incidence of Na D ISM as functions of star-formation properties (Section 5.1.1), dust attenuation (Section 5.1.2), star formation history (Section 5.1.3) and the presence of AGN (Section 5.1.4).

5.1.1. Dependence on star-formation properties

Figure 2 shows the distribution of the sample galaxies on the M_* -sSFR diagram. We find that most Na D ISM (61/72, 85%) are detected in galaxies with $\log(M_*/M_\odot) > 10$, spanning the full range from above to below the star-forming main sequence. In contrast, at the lower-mass end ($\log(M_*/M_\odot) \leq 10$), Na D ISM detections are found only in galaxies on or above the main sequence. We divide our sample galaxies into four subgroups based on their locations on the M_* -sSFR plane, separated by $\log(M_*/M_\odot) = 10$ and $\log(\text{sSFR}/\text{yr}^{-1}) = -10$. To control for observational bias in the detectability of Na D absorption, which depends strongly on the continuum SNR around Na D, $\text{SNR}_{\text{NaD,cont}}$, we further divide the sample into two subsamples at $\text{SNR}_{\text{NaD,cont}} = 15$, above which we find the detection rate approximately plateaus.

As Figure 3 shows, in the high-SNR subsample, the Na D detection rate is $71 \pm 8\%$ in the high- M_* & low-sSFR region and $39 \pm 10\%$ in the high- M_* & high-sSFR region, while much lower in the “low- M_* & high sSFR” region ($7 \pm 2\%$). A qualitatively similar pattern is seen in the low-SNR subsample, where the Na D detection rate is highest in the high- M_* & low-sSFR region ($40 \pm 8\%$) and decreases to $16 \pm 4\%$ in the high- M_* & high-sSFR region. In the low- M_* subgroups, the sample sizes are too small to constrain the incidence. The similar incidence pattern in the high- M_* regions across the high- and low-SNR subsamples suggests that the dependence of Na D detection on M_* and sSFR is not driven by continuum-SNR-related observational bias. Instead, these results indicate that Na D-traced neutral ISM is much more prevalent in galaxies with high M_* , and that its detection rate in massive galaxies below the main sequence is comparable to, or even slightly higher than, that in massive star-forming galaxies.

We also perform a spectral stacking analysis for galaxies with and without Na D detections. Each galaxy spectrum is first normalized by its pPXF-derived stellar continuum (Section 4.1). When present, the nearby He I $\lambda\lambda 5877$ emission is subtracted before stacking using the best-fit model from Section 4.2. We then construct the stacked Na D spectra using inverse-variance weighting. We have verified that median stacking yields the same qualitative conclusions.

Figure 4 shows the stacked spectra of Na D-detected and undetected galaxies in the four subgroups. Overall, the stacked spectra of Na D-undetected galaxies do not show clear Na D ISM absorption, except in the high- M_* and high-sSFR subgroup, where the stacked spectrum of 79 galaxies shows tentative Na D ISM absorption at $\sim 1.5\sigma$. These results indicate that our measured Na

D ISM incidence rates are broadly robust, with no clear evidence that galaxies with strong Na D ISM absorption are being missed by our analysis.

Taking a closer look at the stacked line profiles of the Na D ISM detected galaxies, we find that the two high- M_* subgroups show deeper absorption than the “low- M_* & high-sSFR” subgroup, suggesting that the neutral ISM is more abundant in massive galaxies than in low-mass galaxies. Moreover, between the two high- M_* subgroups, both stacked profiles are blueshifted, but the profile of the high-sSFR subgroup is narrower than that of the low-sSFR subgroup.

The narrower Na D absorption profile seen in the “high- M_* & high-sSFR” subgroup can be explained in two ways. First, the Na D ISM absorptions in this subgroup may be more predominantly systemic or blueshifted than those in the “high- M_* & low-sSFR” subgroup. This interpretation is supported by our observations: we find only one inflow in the “high- M_* & high-sSFR” subgroup, whereas 5 out of 39 Na D ISM detections in the “high- M_* & low-sSFR” subgroup are redshifted. These redshifted absorbers therefore contribute substantially to the red absorption wing of the stacked profile in the “high- M_* & low-sSFR” subgroup, making the absorption appear broader. Alternatively, the spectra considered here have only moderate resolution. If redshifted Na D emission is present at a non-negligible level, it may partially fill in an intrinsically broad absorption profile, causing the observed Na D profile to appear narrower. This second scenario is also plausible, as A. Concas et al. (2019) showed that the stacked Na D profile of massive star-forming galaxies in the local Universe can be reproduced only by including a redshifted emission component in addition to blueshifted Na D absorption.

5.1.2. Dependence on dust

We now examine how the incidence of Na D ISM absorption depends on dust attenuation, a physical property that has been found to govern the amount of Na D-traced neutral gas in the local Universe (e.g., Y.-M. Chen et al. 2010; D. Poznanski et al. 2012).

Considering the full sample, the median A_V of the Na D ISM-detected galaxies is higher than that of the undetected ones, with median values of 2 and 1 mag, respectively. For the Na D ISM-detected subsample, we test the correlation between A_V and the equivalent width of the Na D ISM absorption, $\text{EW}_{\text{NaD,ISM}}$. As shown in Figure 5, we find a strong positive correlation between these two quantities. A Spearman rank test confirms this correlation to be statistically significant with $p \ll 0.05$.

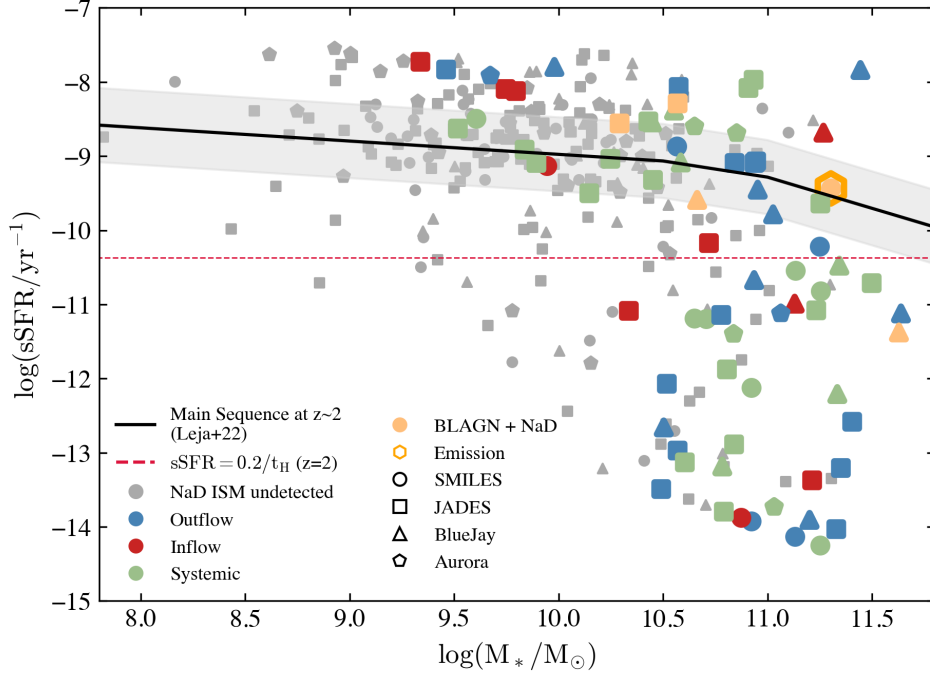


Figure 2. SED-derived SFR versus galaxy stellar mass diagram. Galaxy sample from SMILES, JADES, Blue Jay, and Aurora are marked by circles, squares, triangles, and pentagons, respectively. Gray points are galaxies without Na D ISM detection. Na D outflow, inflow, and systemic ISM are represented by blue, red, and green colors, respectively. Five broad-line AGN with Na D ISM detections are shown in yellow; one of them – SMILES-196290, which exhibits Na D emission – is highlighted with an orange hexagon outline. The black line with gray-shaded regions shows the star-forming main sequence (SFMS) at $z \sim 2$ from J. Leja et al. (2022), with a scatter of 0.5 dex. The massive quiescent galaxies selected by $\Delta MS < -0.5$ dex are also generally located below $sSFR < 0.2/t_H$ at $z \sim 2$ (red dashed line), another commonly used quiescent selection criterion (A. C. Carnall et al. 2018; W. M. Baker et al. 2025a).

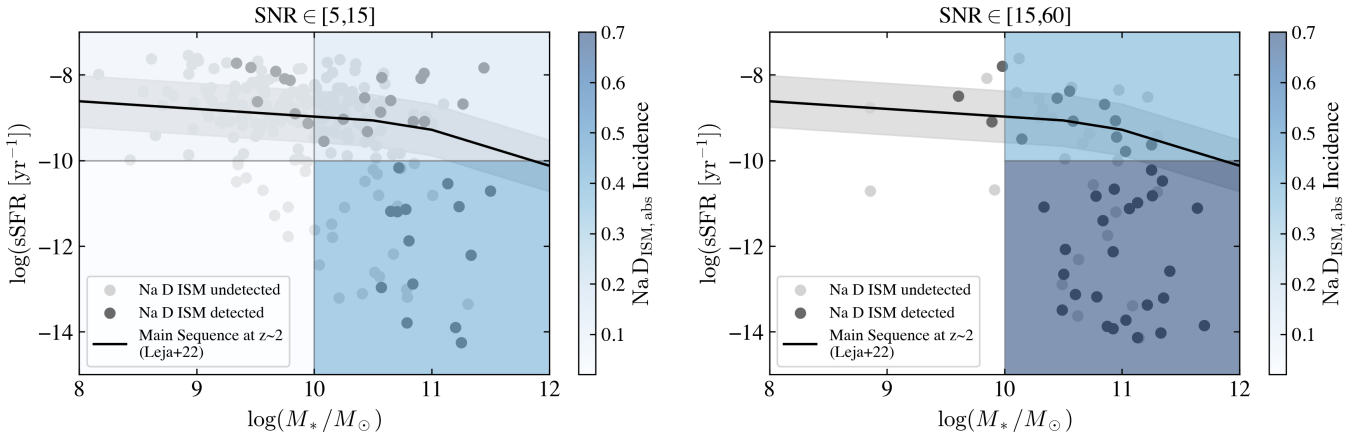


Figure 3. The Na D ISM incidence across the M_* -sSFR plane. Galaxies with low-SNR and high-SNR continuum detections around Na D are shown in the left and right panels, respectively. The light-gray and dark-gray points represent the galaxies with and without Na D ISM detection, respectively. The black line with gray shaded regions shows the star-forming main sequence (SFMS) at $z \sim 2$, same as the line shown in Figure 2. The whole M_* -sSFR plane is split into four regions by $\log(M_*/M_\odot) = 10$ and $\log(sSFR[\text{yr}^{-1}]) = -10$, and then color-coded by the Na D ISM incidence within the region.

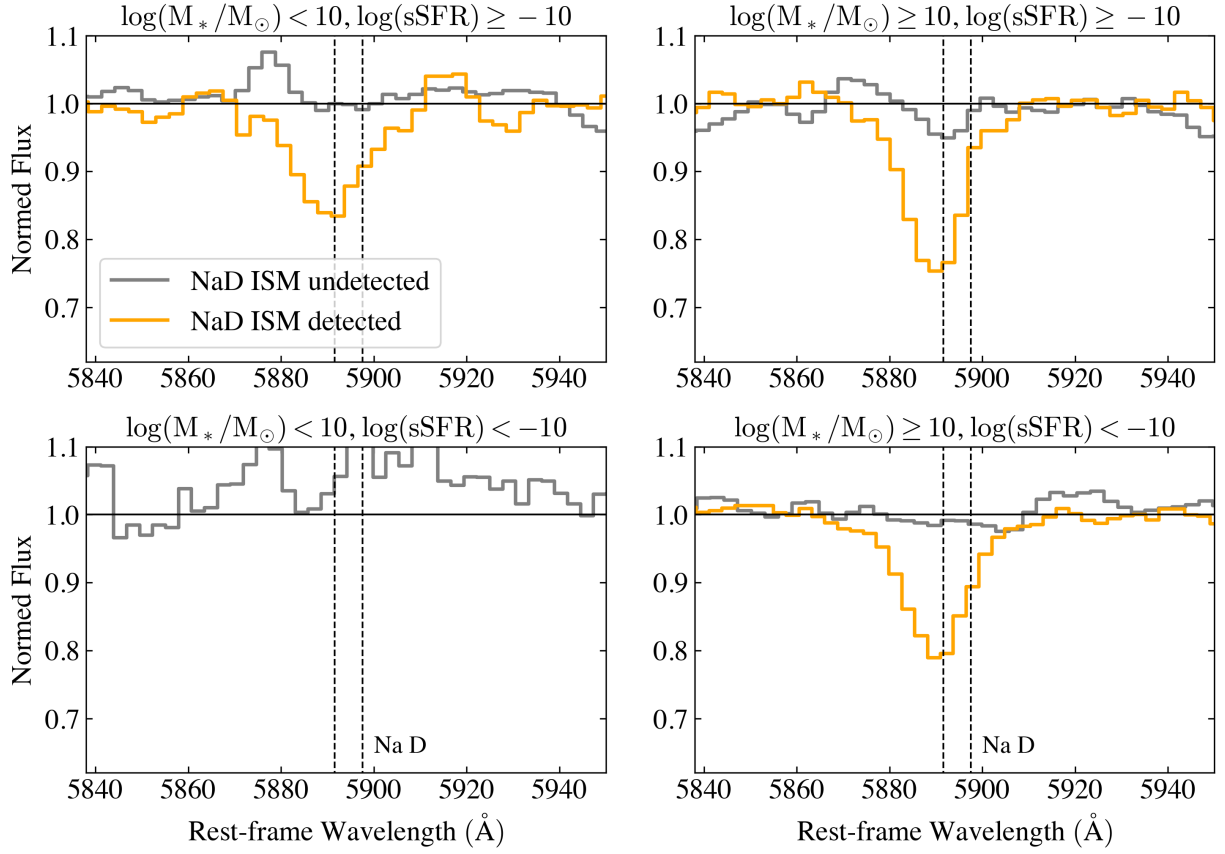


Figure 4. The stacked Na D residual spectrum (stellar component removed) of galaxies at four different M_* -sSFR regions. The spectra of Na D ISM-detected and undetected galaxies are shown as orange and gray lines, respectively.

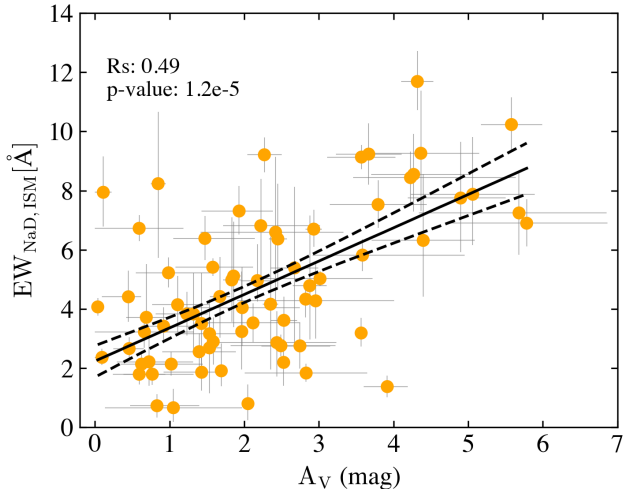


Figure 5. Equivalent width of the Na D ISM absorption component, $EW_{\text{NaD,ISM}}$, as a function of A_V . The solid line shows the best-fit log-linear relation and the dashed lines show the 90% confidence intervals. The strong correlation between $EW_{\text{NaD,ISM}}$ and A_V is confirmed by a Spearman rank test with $R_s = 0.49$ and $p \ll 0.05$.

These results indicate that the presence of Na D-traced ISM strongly depends on dust attenuation.

In Figure 6, we further compare the A_V distributions of the four subgroups across different regions of the M_* –sSFR plane, where we also perform K-S tests on the A_V distributions of the detected and undetected subsamples. For the two high-sSFR subgroups, regardless of stellar mass, the median A_V of the Na D ISM-detected galaxies is higher than that of the undetected galaxies by about 1 mag. In both cases, the K-S test returns $p < 0.05$, indicating that the two A_V distributions are different. These results suggest that dust attenuation is a key factor governing the detectability of Na D ISM in star-forming galaxies. This can be understood because Na D has a low ionization potential of 5.14 eV and requires substantial dust shielding to survive radiation from intense star-formation or AGN activity.

In contrast to the high-sSFR subgroups, the A_V distributions of the Na D ISM-detected and undetected galaxies in the “high- M_* & low-sSFR subgroup” are similar. The median A_V values are 1.7 and 1.5 mag for the detected and undetected subsamples, respectively, and the K-S test indicates that the two distributions are statistically indistinguishable. In addition, the A_V of Na D-detected massive quiescent galaxies is also comparable to that of Na D ISM-undetected massive star-forming galaxies (see the right column of Figure 6). Taken together, these results suggest that, unlike in star-forming galaxies, the detectability of Na D ISM absorption in massive quiescent systems is not primarily controlled

by dust attenuation, but instead by other physical factors that we examine in the next section (Section 5.1.3). It is also worth noting that, although the “high- M_* & low-sSFR” subgroup generally has lower A_V than the “high- M_* & high-sSFR” subgroup, its A_V distribution exhibits a long tail toward high values. This suggests that a non-negligible fraction of cosmic-noon quiescent galaxies still retain substantial amounts of dust, consistent with recent studies reporting dusty quiescent systems in the early Universe (J. C. Siegel et al. 2025; Z. Ji et al. 2024b).

5.1.3. Dependence on star formation history

Since dust attenuation alone does not explain the presence of Na D ISM absorption in the “high- M_* & low-sSFR” subgroup, we next examine whether quiescent galaxies with and without Na D detections differ in their stellar population properties. We begin with the spectral differences, which are more directly observed and therefore less model dependent, and then interpret them in the context of star-formation history reconstructed from SED fitting (Section 4.4).

To enable a reliable comparison of age-sensitive features, we restrict the sample to galaxies in the “high- M_* & low-sSFR” group with $\text{SNR} > 15$. The middle and bottom rows of Figure 7 show that, on average, the Na D-detected galaxies have a stronger 4000 Å break, as well as stronger Ca H&K and G-band absorption, than the undetected subsample. These features indicate a larger contribution from evolved stellar populations. At the same time, the Na D-detected galaxies also tend to exhibit stronger Balmer absorption. This combination suggests that the Na D-detected population is not uniform: it includes both older systems with prominent metal-line absorption and systems with signatures of relatively recent, rapid quenching.

We quantify these trends using the D_n4000 and $H\delta_A$ indices, following M. L. Balogh et al. (1999) and G. Worthey & D. L. Ottaviani (1997). Both indices are measured from the best-fit stellar component derived with pPXF (Section 4.1), and their uncertainties are propagated using MCMC. Owing to wavelength-coverage and detector-gap limitations, only 25 of the 36 galaxies in this subgroup have usable measurements of both indices. Figure 8 shows the distribution of these 25 galaxies on the D_n4000 – $H\delta_A$ plane, together with FSPS evolutionary tracks for exponentially declining SFHs with $\tau = 0.2, 0.5,$ and 1 Gyr.

Two trends emerge. First, Na D ISM seems to be more common among the quiescent galaxies with larger D_n4000 : 6 of 7 (86%) systems with $D_n4000 > 1.4$ show Na D absorption, compared with 11 of 18 (61%) with

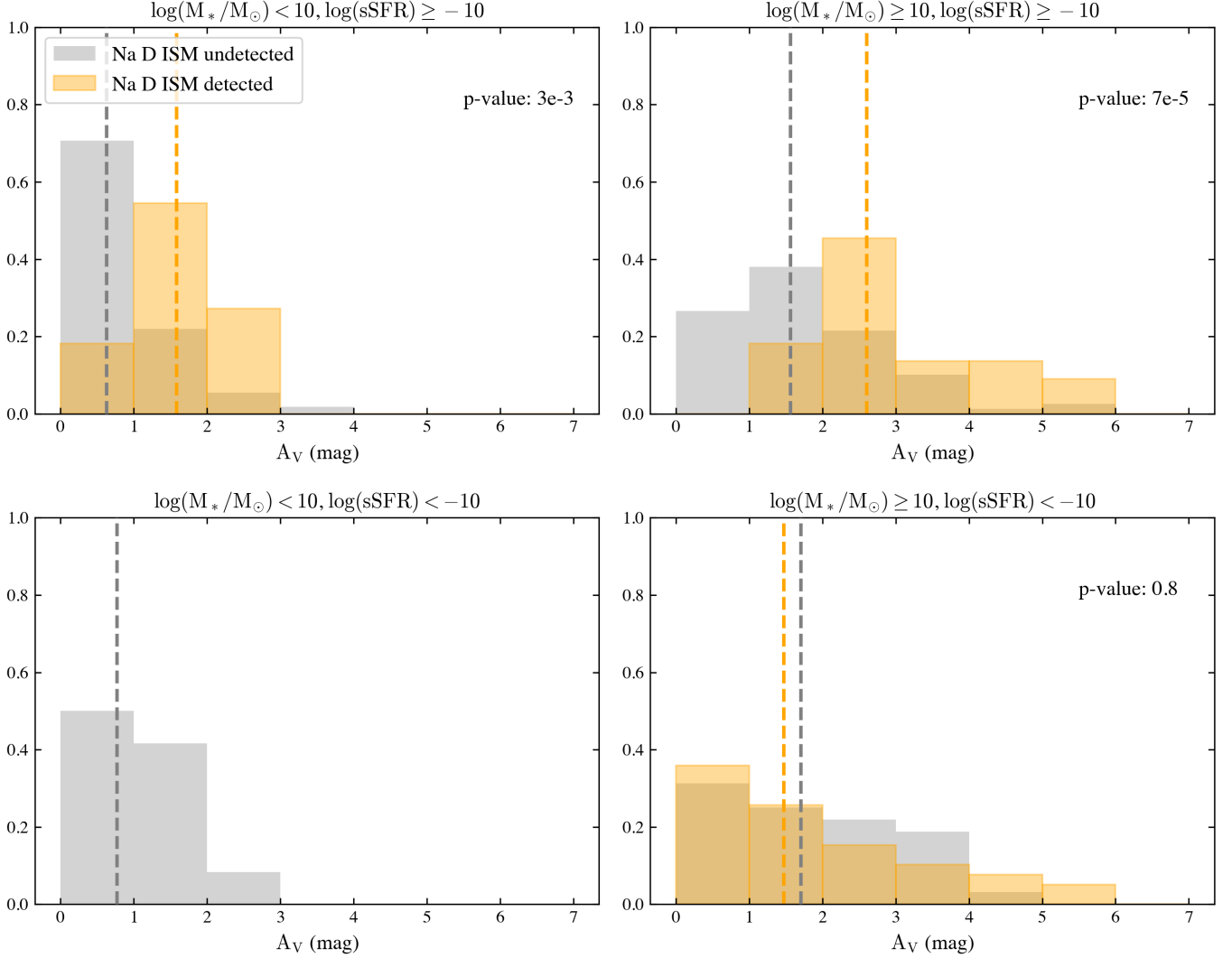


Figure 6. The A_V distribution of Na D ISM detected (orange) and undetected (gray) galaxies at four different M_* -sSFR regions. The median of each distribution is marked by a dashed line. The p-value shown in each panel represents the significance of the K-S test for the difference between the two distributions.

$D_n4000 \leq 1.4$. Second, within the quiescent population with similar D_n4000 (≤ 1.4), the Na D-detected galaxies tend to have larger $H\delta_A$ than the undetected galaxies, placing them closer to tracks with more rapidly declining SFHs. By contrast, the undetected systems generally occupy regions consistent with more gradual decline.

These spectral diagnostics suggest that Na D ISM is preferentially detected in massive quiescent galaxies with two types of star-formation histories: older systems with larger D_n4000 , and younger systems with smaller D_n4000 but stronger $H\delta_A$, indicative of a more rapid shutdown of star formation. This implies that Na D detectability depends not only on the time since quenching, but also on the manner in which quenching occurred.

This interpretation is broadly consistent with the reconstructed SFHs shown in Figure 7. The Na D-detected galaxies more often show an earlier decline in star formation, typically beginning ~ 100 – 1000 Myr ago, whereas the undetected systems tend to show a more recent drop, usually within $\lesssim 100$ Myr. The SFHs also reinforce the diversity implied by the spectral diagnostics, particularly within the detected population.

Finally, the Na D kinematics show a similar dependence on stellar population properties. Most Na D outflows (7/8) are found in the younger massive quiescent galaxies with high $H\delta_A$; and among young quiescent galaxies with Na D detections, the absorption is predominantly outflowing (7/11). This suggests that Na D kinematics, especially outflows, are also linked to recent quenching history. We discuss the physical origin

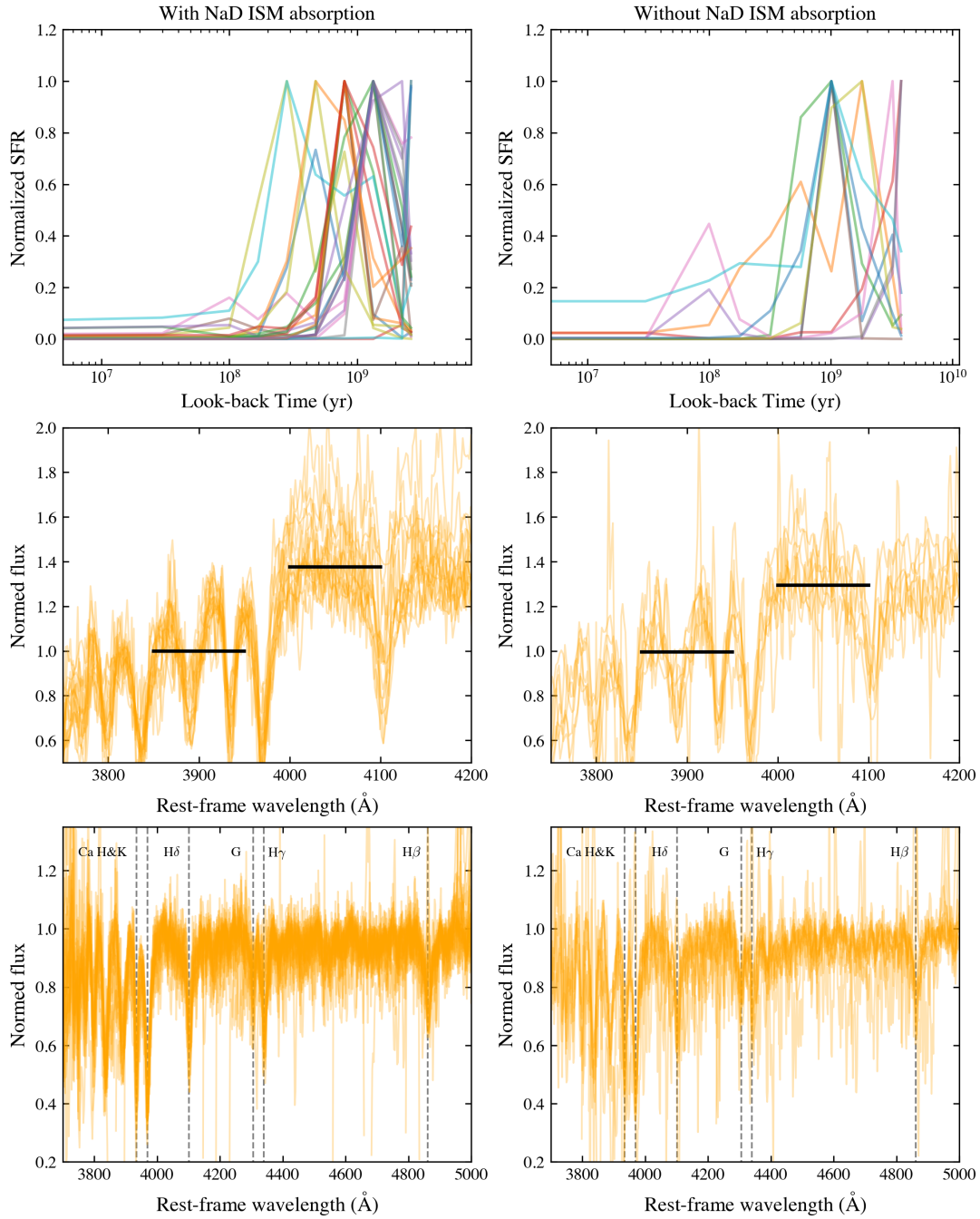


Figure 7. Comparison of stellar population properties between Na D ISM absorption detected (left) and undetected (right) massive quiescent galaxies. **Top:** Reconstructed non-parametric SFH of each individual galaxy. Each SFH is normalized to its own maximum SFR across the nine time bins. **Middle:** Observed NIRSpect/MSA $R \sim 1000$ spectrum around 4000\AA break of each individual galaxy. The black horizontal lines represent the average fluxes within the two continuum windows ($3850\text{--}3950\text{\AA}$ and $4000\text{--}4100\text{\AA}$) for $D_n 4000$ calculation. Since each spectrum is normalized to its average continuum flux on rest-frame $3850\text{--}3950\text{\AA}$, a higher value in the red continuum windows means a stronger 4000\AA break. **Bottom:** $H\delta$ -to- $H\beta$ absorptions of each individual galaxy, normalized by a smoothing-spline fit. The dashed grey lines mark the locations of Ca H&K, $H\delta$, G-band, $H\gamma$, and $H\beta$. Overall, Na D-detected quiescents span both older systems with stronger 4000\AA breaks, Ca H&K, and G-band features, and younger, rapidly quenched (PSB-like) systems with stronger Balmer absorption.

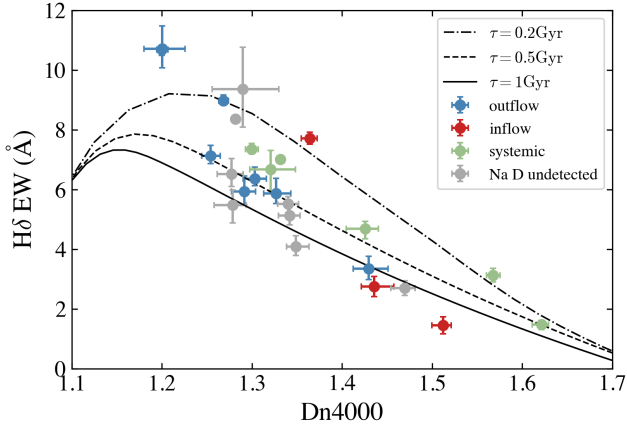


Figure 8. Massive quiescent galaxies in the $H\delta_A$ vs. D_n4000 diagram. The symbols are the same as Figure 2. The black reference lines from top to bottom are tau-model SFH with $\tau = 0.2, 0.5,$ and 1 Gyr, respectively. The Na D ISM is preferentially detected in either old quiescent galaxies with $D_n4000 > 1.4$, or in young, rapid-quenching ($\tau = 0.2$ and 0.5 Gyr) galaxies with larger $H\delta_A$ and behaves as an outflow.

of the dependence of Na D detectability and kinematics on dust and quenching history in Section 6.4.

5.1.4. Dependence on AGN presence

We next examine whether the detectability and kinematics of Na D-traced ISM depend on AGN activity. We identify AGN primarily using optical emission-line diagnostics based on the [N II]-BPT (J. A. Baldwin et al. 1981) and [S II]-VO87 (S. Veilleux & D. E. Osterbrock 1987) diagrams, using the line ratios [O III]/H β , [N II]/H α , and [S II]/H α . Line ratios are treated as upper or lower limits when the numerator or denominator line has SNR < 3, respectively, and galaxies with only tentative detections in both lines are excluded from the diagnostic diagrams.

We classify a galaxy as AGN-hosting if its line ratios lie in the AGN region of either diagram. We do not classify galaxies in the “composite” region of the [N II]-BPT diagram or the “LINER” region of the [S II]-VO87 diagram as AGN, although these systems may still contain some AGN contribution. In addition, since AGN can also be identified through multiwavelength signatures beyond optical line-ratio diagnostics, we further supplement the optical classification with broad-line identifications (R. L. Davies et al. 2024; Y. Sun et al. 2025; I. Juodžbalis et al. 2026), X-ray detections (Y. Q. Xue et al. 2016; B. Luo et al. 2017), and mid-IR AGN selections (J. Lyu et al. 2022, 2024) from the literature, thereby constructing a more complete AGN census.

Under this selection, the AGN incidence among Na D ISM-detected galaxies is $35 \pm 6\%$, only modestly higher

than the $22 \pm 3\%$ in the undetected sample, implying that AGN presence is not the exclusive factor governing the detectability of Na D-traced neutral ISM. The trend with Na D kinematics is stronger: the AGN incidence rises from 10% (1/10) in the inflow subsample to 36% (12/33) in the systemic subsample and 46% (12/26) in the outflow subsample. This suggests that AGN activity is more strongly associated with the kinematic state of the NaD-traced ISM, especially the presence of outflows. We will further examine the role of AGN in driving outflows across different galaxy populations in Section 5.2.

5.2. Neutral outflow in cosmic-noon galaxies

In this section, we investigate the Na D outflow-detected galaxies in our sample, focusing on their properties, the mechanisms that may drive them, and their dependence on host-galaxy and AGN characteristics.

5.2.1. Na D outflow properties

Following Y. Sun et al. (2026), we derive the physical properties of the Na D outflows based on the Na D profile modeling described in Section 4.2. These include the outflow velocity (V_{out}), mass and mass outflow rate (M_{out} and \dot{M}_{out}), momentum and momentum outflow rate (p_{out} and \dot{p}_{out}), and energy and energy outflow rate (E_{out} and \dot{E}_{out}). We define the outflow velocity as $v_{\text{out}} = |\Delta v| + 2\sigma$, where $\sigma = b/\sqrt{2}$ is the velocity dispersion of the Na D ISM line.

We compute the mass outflow rate as

$$\begin{aligned} \dot{M}_{\text{out}} &= \frac{M_{\text{out}} v_{\text{out}}}{r_{\text{out}}} \\ &= 11.45 \left(C_{\Omega} \frac{C_f}{0.4} \right) \left(\frac{N(\text{H I})}{10^{21} \text{ cm}^{-2}} \right) \\ &\times \left(\frac{r_{\text{out}}}{1 \text{ kpc}} \right) \left(\frac{v_{\text{out}}}{200 \text{ km s}^{-1}} \right) M_{\odot} \text{ yr}^{-1}, \end{aligned}$$

assuming outflow extent $r_{\text{out}} = 1$ kpc and covering factor related to the wind opening angle $C_{\Omega} = 0.5$. The hydrogen column density $N(\text{H I})$ is inferred from $N(\text{Na I})$ assuming Milky-Way-like Na abundance and dust depletion, together with a neutral fraction of 10% (D. S. Rupke et al. 2005b). We derive $N(\text{Na I})$ from the best-fit central optical depth ($\tau_{r,0}$) of the red Na D line:

$$\begin{aligned} N(\text{Na I}) &= 10^{13} \left(\frac{\tau_{r,0}}{0.758} \right) \left(\frac{0.4164}{f_{lu}} \right) \\ &\times \left(\frac{1215 \text{ \AA}}{\lambda_{lu}} \right) \left(\frac{b}{10 \text{ km s}^{-1}} \right) \text{ cm}^{-2}, \end{aligned}$$

where $f_{lu} = 0.32$ and $\lambda_{lu} = 5897.55 \text{ \AA}$.

Uncertainties in the outflow properties are propagated from the MCMC fitting of the Na D profile parameters.

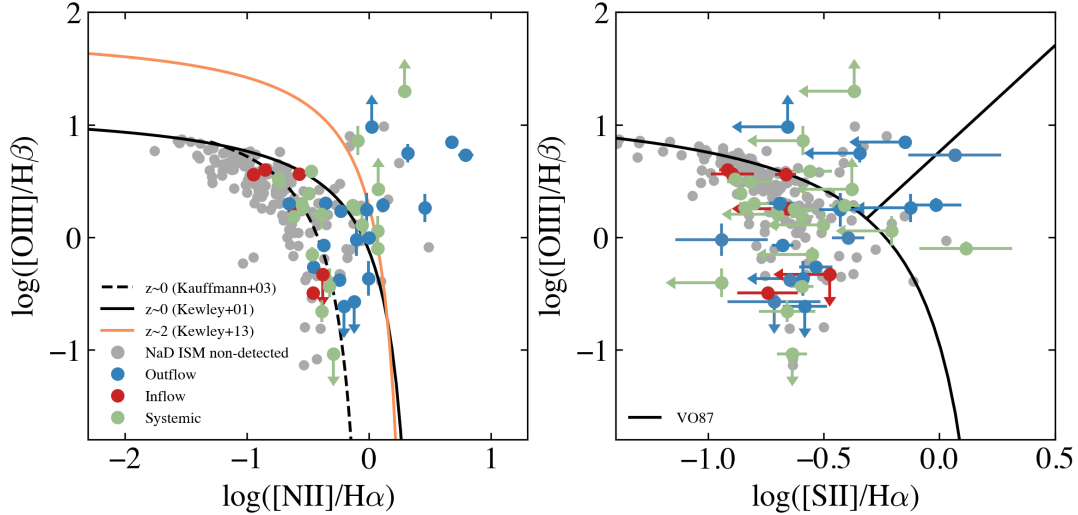


Figure 9. Distribution of parent galaxies in the [N II]-BPT diagram (left) and [S II]-VO87 diagram (right). As in Figure 2, gray points are galaxies without Na D ISM detection, and Na D outflow, inflow, and systemic ISM are represented by blue, red, and green colors, respectively. The black solid, black dashed, and orange line in the left panel represents the SF-AGN boundary from G. Kauffmann et al. (2003), L. J. Kewley et al. (2001), and L. J. Kewley et al. (2013), respectively; The black lines in the right panel are from S. Veilleux & D. E. Osterbrock (1987).

However, the systematic uncertainty in \dot{M}_{out} is substantially larger, mainly owing to assumptions about the neutral fraction and C_{Ω} , and is estimated to be ~ 0.6 dex (R. L. Davies et al. 2024; Y. Sun et al. 2026). In addition, the outflow radius r_{out} is unconstrained by the NIRSpec/MSA data, which probe only the central regions of galaxies. The reported \dot{M}_{out} values should therefore be regarded as lower limits, and more accurate measurements will require IFU observations. For example, IFU data for JADES-197911 from GA-NIFS survey¹⁵ show a larger Na D outflow extent ($r_{\text{out}} \sim 2.7$ kpc) and correspondingly higher \dot{M}_{out} ($\sim 60 M_{\odot} \text{yr}^{-1}$, F. D’Eugenio et al. 2024b; J. Scholtz et al. 2026) than our estimate ($\sim 16 M_{\odot} \text{yr}^{-1}$).

From M_{out} and \dot{M}_{out} , we further derive the momentum and energy outflow rates. The measured properties of the 26 Na D outflows are listed in Table A4.

In the following subsections, we examine how V_{out} , \dot{M}_{out} , \dot{E}_{out} , and mass-loading factor ($\eta = \dot{M}_{\text{out}}/\text{SFR}$) correlate with host-galaxy properties. For this purpose, we divide the outflow-detected sample into star-forming and quiescent subsamples based on their relative distance from the star-forming sequence, ΔMS : galaxies with $\Delta\text{MS} > -0.5$ dex are classified as star-forming, while those with $\Delta\text{MS} \leq -0.5$ dex are classified as quiescent.¹⁶ The host classification is listed in Table A4.

¹⁵ <https://ga-nifs.github.io/>

¹⁶ We verify that this quiescent subsample is also consistent with the commonly adopted criterion $\text{sSFR} < 0.2/t_{\text{H}}$ (M. Franx et al. 2008; A. C. Carnall et al. 2018; W. M. Baker et al. 2025a;

In addition to M_* , SFR, and sSFR, we also consider the SFR surface density, $\Sigma_{\text{SFR}} = \text{SFR}/(2\pi R_{\text{eff}}^2)$, and the circular velocity, $V_{\text{cir}} = \sqrt{(GM_*)/(2R_{\text{eff}})}$, which trace the intensity of star formation and the depth of the gravitational potential, respectively. Here, we use the R_{eff} measurements reported by A. Genin et al. (2025), based on JWST/NIRCam imaging.

5.2.2. Outflow velocity and mass outflow rate

Figure 10 shows the relation between V_{out} and the aforementioned host-galaxy properties, together with the Spearman correlation coefficients and p -values.

To begin, we find no clear correlation between V_{out} and either M_* (panel a) or V_{cir} (panel b). Nevertheless, nearly all Na D outflows satisfy $V_{\text{out}} < 3V_{\text{cir}}$, where $3V_{\text{cir}}$ is commonly adopted as an approximation to the escape velocity (S. Veilleux et al. 2005). This suggests that most Na D outflows, particularly those in galaxies with deep potential wells, are unlikely to escape and instead remain gravitationally confined, whereas the outflows in the three systems with relatively shallow potential wells in our sample ($\log(V_{\text{cir}}/\text{km s}^{-1}) < 2.4$) may reach the CGM/IGM.

Panels c–e of Figure 10 show how V_{out} varies with star-formation activity. In the quiescent subsample, V_{out} shows no clear relation with SFR, sSFR, or Σ_{SFR} . By contrast, the star-forming subsample shows weak posi-

Z. Ji et al. 2026), and recover the spectroscopically confirmed quiescent galaxies in JADES (W. M. Baker et al. 2025b) and Blue Jay (M. Park et al. 2024).

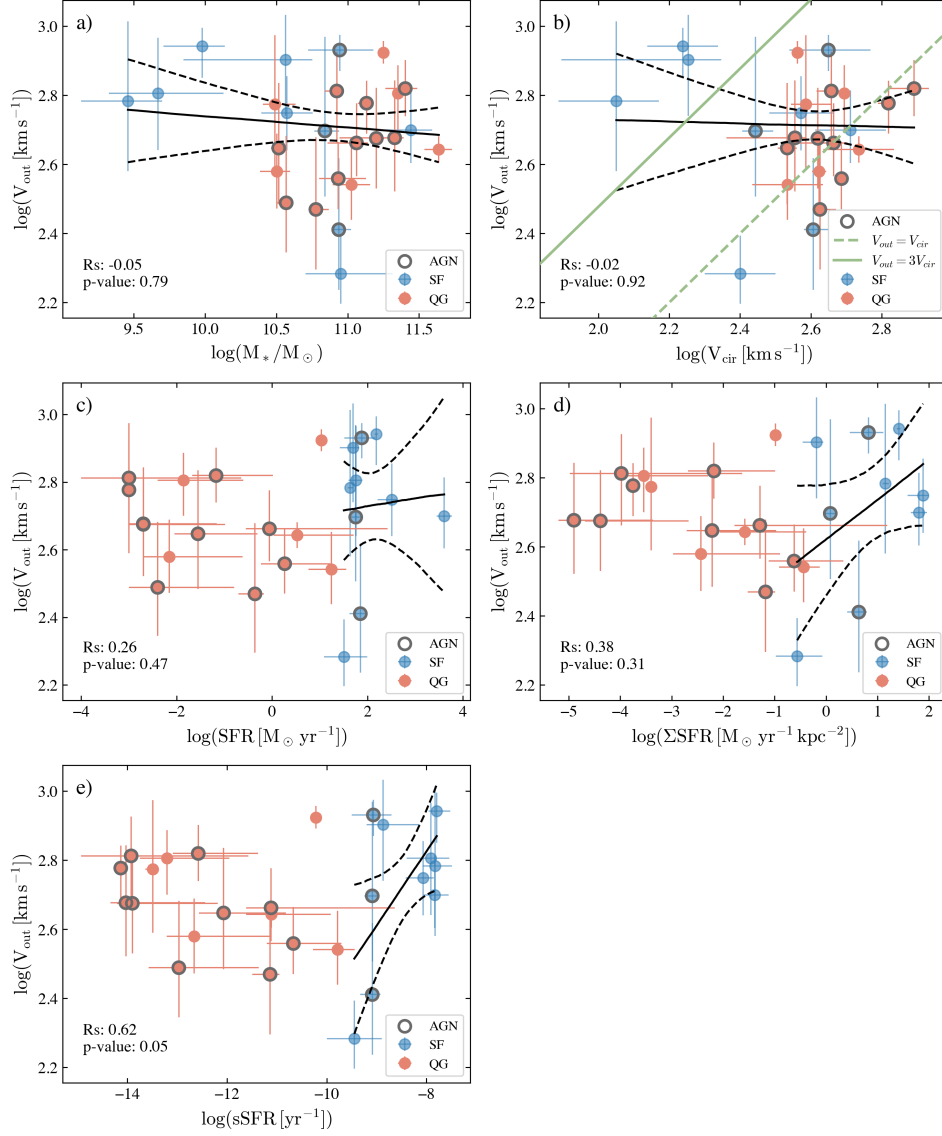


Figure 10. Outflow velocity V_{out} as a function of M_* , V_{cir} , SFR, ΣSFR , and sSFR. The Na D outflow sample is divided into the quiescent ($\Delta\text{MS} \leq -0.5$ dex, red) and star-forming galaxies ($\Delta\text{MS} > -0.5$ dex, blue). AGN hosts are outlined in grey. In each panel, the solid black line shows the best-fit log-linear relation and the dashed lines indicate the 90% confidence interval. The regression is performed using the full outflow sample for the M_* , V_{cir} trends, while using only the star-forming subsample for the star-formation indicators (SFR, ΣSFR , and sSFR). The Spearman coefficient and the corresponding p-value are shown in each panel.

tive trends between V_{out} and all three quantities, with Spearman coefficients of $R_S \sim 0.3\text{--}0.4$. Among these, only the $V_{\text{out}}\text{--sSFR}$ relation reaches formal significance ($p \sim 0.05$), while the trends with SFR and ΣSFR are not statistically significant. Larger samples will be needed to assess these trends more robustly.

Similarly, Figure 11 shows no clear dependence of \dot{M}_{out} on M_* , nor any obvious correlation with star-formation properties in the quiescent subsample. In contrast, the star-forming subsample exhibits moderately positive trends of \dot{M}_{out} with SFR, ΣSFR , and sSFR

($R_S \sim 0.3\text{--}0.5$), although larger samples are needed to confirm these relations. A similar distinction is seen in the mass-loading factor η , shown in panel b of Figure 11. In star-forming galaxies, η is generally around or below unity, consistent with expectations for star formation-driven outflows (e.g., R. Davé et al. 2011; R. S. Somerville et al. 2015). By contrast, the quiescent subsample mostly lies above $\eta = 1$, implying that these outflows can remove cool gas faster than it is consumed by star formation. Such elevated mass-loading factors are more commonly associated with AGN-driven

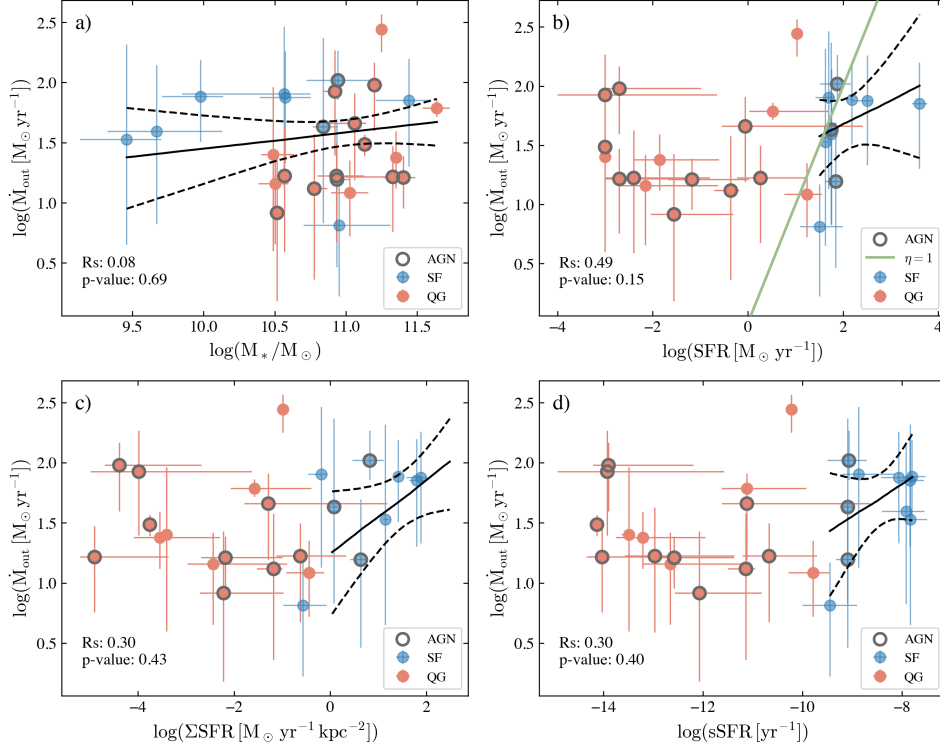


Figure 11. Mass outflow rate \dot{M}_{out} as a function of M_* , SFR, ΣSFR , and sSFR. The symbols are the same as Figure 10. Again, the regression is performed using the full outflow sample for the M_* trend, while using only the star-forming subsample for the star formation indicators (SFR, ΣSFR , and sSFR). The green line in panel b represents the case when mass loading factor $\eta = 1$ (i.e., \dot{M}_{out}), which is the maximum value predicted for “SF-driven” outflows.

outflows, for which η can be enhanced by one or even two orders of magnitude (e.g., E. González-Alfonso et al. 2017).

Taken together, the trends in V_{out} and \dot{M}_{out} are consistent with Na D outflows in star-forming galaxies being primarily driven by ongoing star formation, whereas those in quiescent galaxies likely require a different driving mechanism (e.g. AGN).

5.2.3. Energy and momentum outflow rates

The different trends seen for star-forming and quiescent galaxies in the previous section suggest that their Na D outflows may arise from different launching mechanisms. We therefore examine this issue in terms of energy and momentum outflow rates, by comparing the observed Na D outflows with the energy and momentum that can be supplied by ongoing star formation and AGN activity. Since these are the two main processes capable of driving strong galactic outflows (A. King & K. Pounds 2015; D. S. N. Rupke 2018), we estimate their expected output rates in this section.

We estimate the energy available from current star formation from the star-formation luminosity, $L_{\text{SF}} \approx \text{SFR}_{\text{SED}} \times 10^{10} L_{\odot}$, and the corresponding momentum input as L_{SF}/c . For galaxies classified as AGN, we es-

timate the AGN luminosity, L_{AGN} , from X-ray fluxes when available, following F. Duras et al. (2020). For X-ray-undetected AGN, we instead adopt the [O III]-based bolometric correction of H. Netzer (2009), $L_{\text{bol}} = 600 L_{[\text{O III}]}$, while noting that such estimates are uncertain because $L_{[\text{O III}]}$ depends on obscuration and the physical conditions of the narrow-line region (A. M. Diamond-Stanic et al. 2009; A. Pennell et al. 2017; H. Netzer 2019). The corresponding AGN momentum input is taken to be L_{AGN}/c .

Figure 12 compares the measured energy and momentum rates of the Na D outflows with the expected contributions from star formation and AGN. For star formation, we adopt the reference relations for supernova-driven winds from S. Veilleux et al. (2005), based on solar-metallicity Starburst99 models (C. Leitherer et al. 1999): $\dot{E}_{\text{SN}} = 7 \times 10^{41} \text{SFR erg s}^{-1}$ and $\dot{p}_{\text{SN}} = 5 \times 10^{33} \text{SFR dyne}$. For AGN-driven outflows, theoretical expectations suggest that, in the energy-conserving case, the kinetic power can reach $\sim 5\%$ of L_{AGN} and the momentum rate up to $\sim 20 L_{\text{AGN}}/c$, whereas in the momentum-conserving case the momentum rate is expected to be comparable to L_{AGN}/c (A. King & K. Pounds 2015).

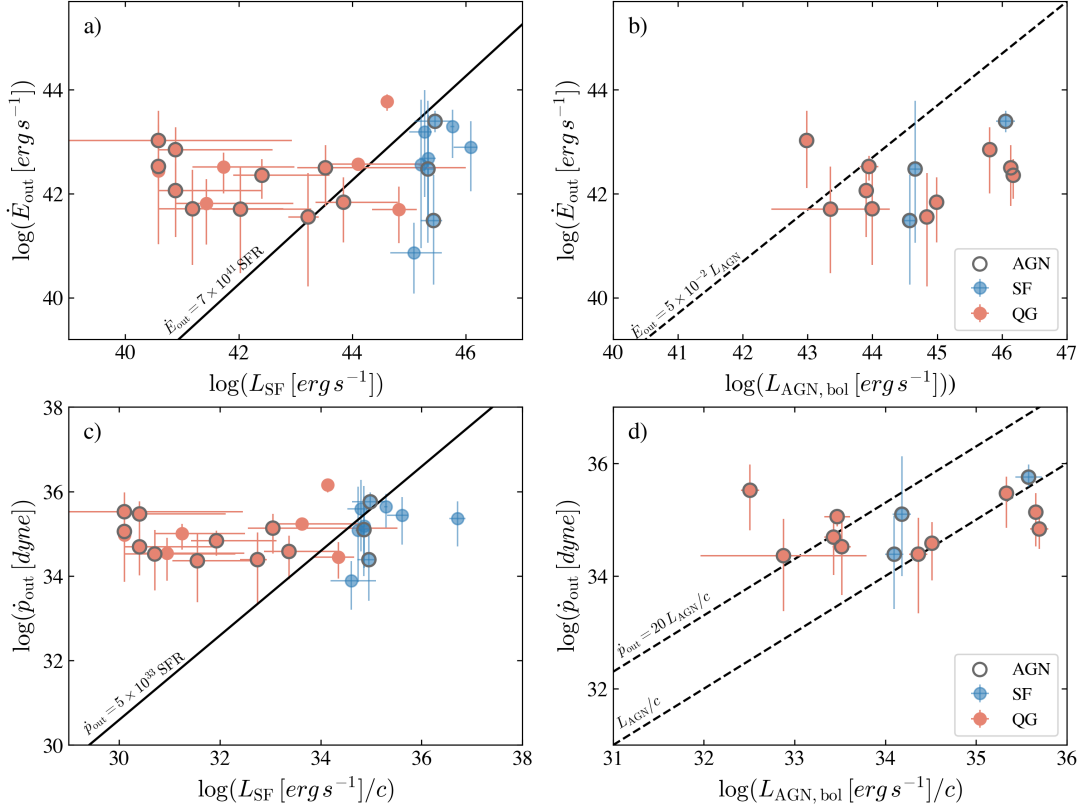


Figure 12. Energy outflow rate \dot{E}_{out} and momentum outflow rate \dot{p}_{out} of $z \sim 2$ Na D outflows compared to the SF (left) and AGN luminosity (right). The symbols are the same as Figure 10 and 11. The black solid lines on the left column represent the expected outflow kinetic energy driven by star formation, and the black dashed lines on the right column represent the typical \dot{E}_{out} values for AGN-driven winds, and \dot{p}_{out} for AGN energy-driven ($20L_{\text{AGN}}/c$) and momentum driven winds (L_{AGN}/c).

The left column of Figure 12 shows that the Na D outflows in star-forming galaxies all have \dot{E}_{out} below the energy injection rate expected from their current star formation, indicating that ongoing star formation can plausibly power these neutral outflows. The same conclusion is supported by the momentum-rate comparison. In contrast, most quiescent galaxies lie above the maximum energy and momentum that their current star formation could provide, implying that their weak ongoing star formation is insufficient to drive the observed Na D outflows.

AGN are a plausible power source for many of the Na D outflows in quiescent galaxies. AGN are present in 10/16 (63%) of the quiescent outflow hosts, much higher than 3/10 (30%) of the outflow-detected star-forming subsample. The outflows in those AGN hosts typically have $\dot{E}_{\text{out}} < 0.05L_{\text{AGN}}$, and their momentum rates lie between the expectations for momentum-conserving and energy-conserving AGN-driven winds, indicating that ongoing AGN activity can plausibly power the outflows in these cases. However, six quiescent galaxies with Na D outflows are not identified as AGN, including SMILES-206183, which hosts the strongest Na D out-

flow currently known at $z > 1$ (Y. Sun et al. 2026). Among them, only BJ-10314 could plausibly be powered by its present-day star formation, perhaps because it lies just below our quiescent threshold ($\Delta\text{MS} = -0.5$ dex). For the remaining five systems, neither instantaneous star formation nor ongoing AGN activity appear sufficient to explain the observed neutral outflows, implying that they likely reflect energy or momentum injected by past activity. We discuss possible driving mechanisms in these systems in Section 6.1.

6. DISCUSSION

With the largest compilation to date of JWST/NIRSpec observations covering Na D at $0.6 < z < 4$, we have carried out a census of Na D-traced neutral ISM and outflows across a broad range of galaxy populations. They are detected primarily in massive galaxies; lower-mass detections are confined to star-forming systems. Behind the mass dependence of Na D ISM incidence, we find that the Na D detectability shows a clear dependence on dust attenuation. In massive quiescent galaxies, we find that it also depends on stellar population properties and quenching history,

being preferentially associated with both older systems and younger, rapidly quenched galaxies. We further identify 26 Na D outflows, and the sources of these outflows appear to differ between star-forming and quiescent hosts.

Motivated by these findings, we further discuss outflow driving mechanisms in detail in Section 6.1. In Section 6.2 we compare neutral and ionized outflows; in Section 6.3 we place the cosmic-noon Na D outflows in the context of local observations; and in Section 6.4 we focus on the implications of Na D-traced neutral ISM for quiescent galaxies.

6.1. Na D Outflow Driving Mechanisms

The physics of Na D-traced neutral outflows at cosmic noon remains poorly constrained. In the local universe, Na D outflows are commonly observed in star-forming galaxies (e.g., D. S. Rupke et al. 2005a; Y.-M. Chen et al. 2010; A. Concas et al. 2019), while their connection to AGN activity remains less clear (e.g., M. Sarzi et al. 2016; A. Concas et al. 2019; D. Baron et al. 2022). At $z \gtrsim 1$, Na D outflows have been identified in quiescent galaxies both with and without clear AGN signatures (R. L. Davies et al. 2024; F. D’Eugenio et al. 2024a; P. G. Pérez-González et al. 2025; F. Valentino et al. 2025; Y. Sun et al. 2026; E. Taylor et al. 2026; P. Zhu et al. 2026), raising the question of whether they are driven by ongoing star formation, current AGN activity, or past feedback episodes. Our census provides important constraints on these possibilities by distinguishing the behavior of Na D outflows in star-forming and quiescent galaxies at $0.6 < z < 4$.

The contrast between the two populations presented in Section 5.2 suggests that Na D outflows at cosmic noon are *not* powered by a single mechanism. In star-forming galaxies, the observed outflow energetics are broadly consistent with the energy and momentum available from ongoing star formation, and the weak positive trends of V_{out} and \dot{M}_{out} with star-formation activity further support a stellar-feedback origin. This implies that the neutral phase traced by Na D is coupled to the same feedback processes that regulate actively star-forming galaxies, and that ongoing star formation can plausibly launch the observed cool outflows.

The situation is very likely different in quiescent galaxies. There, the Na D outflows generally require more energy and momentum than can be supplied by the low level of ongoing star formation, implying that residual star formation is unlikely to be their dominant driver (Figure 12). Many of these quiescent outflows are in galaxies hosting AGN, and in those cases, the observed outflow energetics are broadly consistent with AGN

power. This suggests that Na D outflows in quiescent galaxies trace a mode of feedback that is physically distinct from the star formation-driven winds seen in star-forming systems, and are more directly connected to black hole activity. In this sense, the Na D-traced neutral phase appears able to preserve signatures of AGN feedback even after star formation has already largely ceased.

A particularly interesting result is the presence of six quiescent galaxies without AGN but still with strong Na D outflows (Figure 12), including SMILES-206183, the strongest Na D outflow at $z > 1$ as reported already in Y. Sun et al. (2026). Except for BJ-10314, these outflows are difficult to explain with present-day activity inside the galaxies. Y. Sun et al. (2026) propose the “AGN fossil outflow” scenario to explain the extremely strong Na D outflow in SMILES-206183, in which the observed neutral outflow was launched during an earlier episode of intense AGN activity that has since faded. The same interpretation is plausible for the four newly identified non-AGN quiescent outflows in our sample. A “star-formation fossil outflow” scenario is disfavored because the typical Na D outflow timescale is ~ 10 Myr, assuming an outflow extent of a few kpc and a velocity of $\sim 500 \text{ km s}^{-1}$. This timescale lies well within the youngest 30 Myr bin of our non-parametric SED fitting, so the SED-inferred SFR should already largely reflect the star-formation level at the time when the outflow was launched. By contrast, AGN duty cycles can be significantly shorter than 10 Myr (e.g., K. Schawinski et al. 2015; K. Zubovas et al. 2022), leaving sufficient time for the accretion to shut down while the outflow remains observable. These non-AGN quiescent systems may therefore represent fossil outflows powered by past AGN activity.

This interpretation is in line with other recent studies. E. Taylor et al. (2026) identified three Na D outflows in quiescent galaxies at $z > 2$, and all three have outflow energy rates that exceed the maximum energy available from current star formation or AGN activity. The possibility of fossil outflows is also supported by theoretical modeling, which shows that a substantial fraction of AGN-driven outflows is detectable after the AGN has already shut down (K. Zubovas et al. 2022).

We note that, despite compiling the largest Na D sample at cosmic noon to date, constraining outflow timescales remains difficult, primarily because slit-integrated spectroscopy provides only weak constraints on outflow extent. As a result, the inferred outflow mass, energetics, and timescale remain uncertain. Future spatially resolved IFU observations of Na D outflows in cosmic-noon quiescent galaxies will therefore be essen-

tial for clarifying their physical properties, duty cycles, and connection to galaxy quenching.

In summary, our census supports a picture in which Na D-traced neutral outflows at cosmic noon are state dependent: in star-forming galaxies, their kinematics and energetics are broadly consistent with being powered by ongoing star formation, whereas in quiescent galaxies they are more often linked to AGN feedback, either synchronous in AGN hosts or fossil in systems lacking current AGN signatures. AGN fossil outflows may be common among cosmic-noon quiescent galaxies rather than rare phenomena.

6.2. Comparison with ionized-phase outflows at cosmic noon

Galactic outflows are intrinsically multiphase. In the local Universe, comparisons between ionized outflows and Na D-traced neutral outflows (e.g., C. R. Avery et al. 2022; D. Baron et al. 2022) have shown that, while the ionized phase can reach comparable or higher velocities, the neutral phase often carries a substantially larger outflowing mass. This highlights the importance of comparing different gas phases to understand how feedback redistributes mass, momentum, and energy through galaxies. At cosmic noon, however, population-level multiphase comparisons remain limited, largely because neutral outflow phases have been much harder to observe.

Ionized outflows at cosmic noon have been studied by N. M. Förster Schreiber et al. (2019), who presented a census of [N II]+H α -traced outflows at $0.6 < z < 2.7$ from the KMOS^{3D} survey, distinguishing between “SF-driven” and “AGN-driven” systems. For the SF-driven outflows, they found that the outflow incidence correlates most strongly with Σ_{SFR} . A similar trend is seen in our Na D outflows in star-forming galaxies, where for our star-forming galaxies, the outflow velocity depends on star-formation activity (Figure 10). For the AGN-driven outflows, N. M. Förster Schreiber et al. (2019) found that the incidence depends more strongly on stellar mass, largely because AGN incidence itself increases with stellar mass. Consistent with this, Na D outflows accompanied by AGN signatures in our sample are predominantly hosted by massive galaxies ($\log(M_*/M_\odot) > 10.5$, see Figure 10).

Despite these broad similarities among star-forming galaxies, the neutral and ionized phases differ markedly in the massive quiescent regime. Adopting a consistent quiescent selection of $\log(M_*/M_\odot) > 10$ and $\Delta\text{MS} \leq -0.5$ dex, we find 16 neutral outflows among 42 massive quiescent galaxies (38%), whereas N. M. Förster Schreiber et al. (2019) reported 11 ionized out-

flows among 57 galaxies (19%). This suggests that neutral outflows are more readily detected, and possibly more prevalent, than ionized outflows in massive quiescent galaxies at $z \sim 2$. A likely explanation is tracer-dependent detectability: ionized-outflow identification relies on nebular emission lines and therefore requires sufficiently bright ionized gas, which is often weak in quiescent systems unless they host an AGN or residual star formation. By contrast, Na D absorption uses the stellar continuum as the background source and can therefore trace cooler outflows even in line-weak galaxies. In this sense, Na D is sensitive to a broader range of feedback states, including systems in which the original driving source may already have faded. Indeed, we identify six Na D outflows in quiescent galaxies without AGN signatures, suggesting that neutral outflows can remain observable even when standard ionized-gas diagnostics become ineffective, as discussed in Section 6.1.

We stress, however, that a fair comparison between neutral and ionized outflows ultimately requires a unified galaxy sample with measurements of both phases. Such a census is still missing at $z \sim 2$. One early example comes from the JWST Blue Jay survey, where seven of 16 massive quiescent galaxies show Na D outflows while only three show [O III]-traced ionized outflows (L. Bugiani et al. 2025). With the improved statistics of our Na D census, a future joint analysis of neutral and ionized outflows in a common sample will allow us to quantify their relative incidence, overlap, and correlations across different galaxy populations.

6.3. Comparison with lower-redshift Na D outflows

To explore possible cosmic evolution in Na D outflows, we compare \dot{M}_{out} and \dot{E}_{out} of our $0.6 < z < 4$ sample with those reported in the local Universe. The local comparison samples include Na D outflows in ULIRGs with AGN (D. S. Rupke et al. 2005c), ULIRGs without AGN (D. S. Rupke et al. 2005a; S. Cazzoli et al. 2016), and post-starburst galaxies with AGN (D. Baron et al. 2022). Except for S. Cazzoli et al. (2016), who used spatially resolved spectroscopy, these local measurements were also derived from limited-aperture or long-slit data probing only the central galaxy regions, making them broadly comparable to our JWST/NIRSpec MSA-based measurements.

Figure 13 compares \dot{M}_{out} and \dot{E}_{out} for the Na D outflows at cosmic noon and in the local Universe. The cosmic-noon sample spans $\log(\dot{M}_{\text{out}}[M_\odot \text{ yr}^{-1}]) \sim 0.5$ – 2.5 , with a lower median in quiescent galaxies (~ 1.2) than in star-forming galaxies (~ 1.9). The corresponding $\log(\dot{E}_{\text{out}}[\text{erg s}^{-1}])$ ranges from ~ 40 to 44 , with a smaller difference between the two galaxy populations.

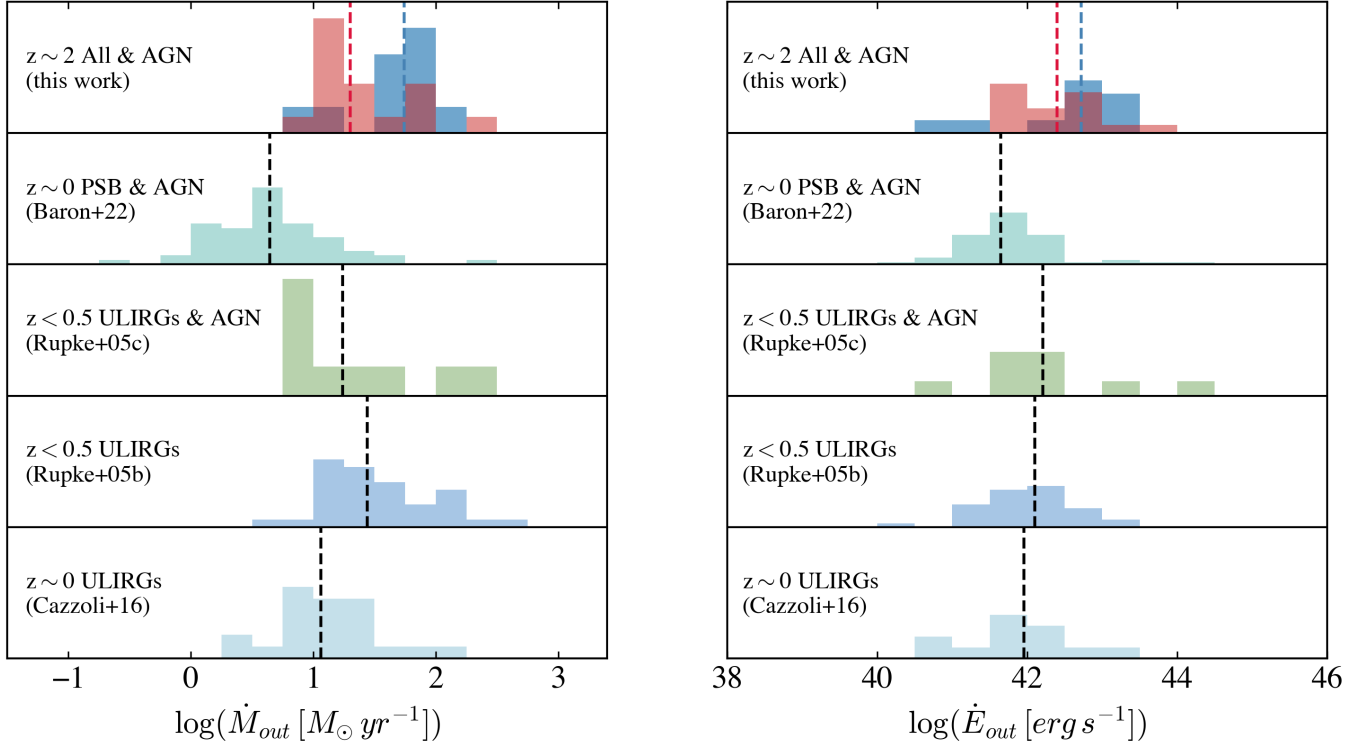


Figure 13. Comparison of neutral Na D outflow properties ($\log(\dot{M}_{\text{out}})$ on the left and $\log(\dot{E}_{\text{out}})$ on the right) in different samples, including 1) the outflows detected in the star-forming (blue) and quiescent (red) at $0.6 < z < 4$ galaxies; 2) the local PSB AGN hosts from D. Baron et al. (2022); 3) the $z < 0.5$ Seyfert-2 ULIRGs from D. S. Rupke et al. (2005c); 4) the $z < 0.5$ SF/LINER ULIRGs from D. S. Rupke et al. (2005a); 5) the local pure-star forming ULIRGs from S. Cazzoli et al. (2016). The median values of each sample are shown by a dashed line. The $\log(\dot{M}_{\text{out}})$ and $\log(\dot{E}_{\text{out}})$ of the $z \sim 2$ Na D outflows appear to be higher than those of the local Na D outflows, but such differences can be mostly attributed to the Na D profile modeling method difference.

Overall, the cosmic-noon Na D outflows appear offset to higher \dot{M}_{out} and \dot{E}_{out} by roughly 0.3–0.5 dex relative to local ULIRGs (D. S. Rupke et al. 2005a,c; S. Cazzoli et al. 2016) and local PSBs (D. Baron et al. 2022). However, we do not interpret this as strong evidence for redshift evolution, because the offset may largely arise from differences in Na D profile modeling. The local studies generally used two ISM kinematic components when required, separating a narrow systemic component from a broader blueshifted outflow component, whereas our analysis adopts a single ISM component because of the limited resolution of the NIRSPEC medium gratings. If a substantial fraction of the absorption in our spectra arises from gas near the systemic velocity, this simplified modeling would overestimate the outflowing mass and energetics. In the limiting case where the systemic and outflowing Na D components contribute comparably, the inferred \dot{M}_{out} would decrease by a factor of two, comparable to the observed offset. We therefore do not regard the current comparison as strong evidence for redshift evolution in Na D outflow properties from $z \sim 0$ to 4. A more robust test will require higher-resolution obser-

vations, such as future NIRSPEC data at higher spectral resolution.

6.4. Na D detectability and outflows in cosmic noon massive quiescent galaxies

In Section 5.1.1, we showed that Na D-traced neutral ISM is widespread in massive quiescent galaxies at cosmic noon. Although larger samples will be needed to confirm the trend, Section 5.1.2 suggests that its detectability also depends on stellar-population properties, with Na D absorption preferentially detected both in older systems with larger D_n4000 and in younger, rapidly quenched galaxies with stronger Balmer absorption (Figures 7 and 8).

A possible interpretation is that the detectability of Na D ISM absorption is governed by a balance between ionization and shielding. In massive quiescent galaxies, after quenching, the cool gas and dust content are often reduced, but the ionizing field also evolves as they age. In recently quenched systems, residual young stars may still produce sufficiently hard UV photons to suppress neutral sodium unless enough shielding remains. As the

stellar population ages and the radiation field softens, Na D absorption can emerge even at relatively modest A_V . This picture naturally explains why Na D is more readily detected in older quiescent galaxies.

However, the presence of Na D ISM in younger quiescent galaxies with strong $H\delta_A$ (Figure 8) suggests that age is not the only factor determining the Na D ISM absorption detectability. In these younger systems, while Na D is generally harder to detect because of their residual UV fields and typically reduced shielding, galaxies that experienced more rapid quenching may still retain or redistribute enough cool neutral gas for Na D absorption to remain visible. In particular, strong feedback associated with rapid quenching may increase the covering fraction of absorbing material, thereby enhancing Na D detectability and producing the outflow signatures we observe. This behavior is broadly consistent with previous studies of post-starburst galaxies at both cosmic noon and in the local Universe: E. Taylor et al. (2024, 2026) found that Na D outflows are preferentially detected in cosmic-noon quiescent galaxies quenched within the past ~ 1 Gyr, while Y. Sun et al. (2024) showed that both the Na D outflow fraction and velocity decline from young to old local post-starburst populations.

Taken together, these results suggest that Na D absorption in massive quiescent galaxies is favored under two conditions: either the stellar population is old enough that the ionizing field has weakened, or quenching was sufficiently recent and rapid that substantial cool gas remains, often in an outflowing configuration. The high incidence of Na D outflows in young, post-starburst-like systems, together with the evidence that AGN may be the primary driver of outflows in quiescent galaxies, points to a close connection between AGN-driven gas removal or redistribution and the quenching process. However, because AGN activity and galaxy quenching operate on very different timescales, our observation cannot establish a direct causal link between them. Still, our identification of fossil AGN outflows suggests that AGN feedback may play an important role in maintaining quiescence after the AGN itself has faded. We detect five potential fossil AGN outflows among 16 quiescent galaxies with Na D outflows, indicating that the impact of AGN feedback can persist well beyond the active phase and may be common among quiescent galaxies at cosmic noon. The continued detectability of these fossil outflows after AGN turn-off in quiescent galaxies suggests that they may keep the gas in a disturbed or heated state, preventing new star formation.

Finally, we caution that the current constraints remain limited by the small number of quiescent galaxies

with robust D_n4000 and $H\delta_A$ measurements. Larger spectroscopic samples at and beyond cosmic noon are needed to better constrain the stellar ages and quenching histories of $z > 1$ quiescent galaxies. In addition, direct measurements of cold gas in quiescent systems beyond the local Universe remain scarce (see Figure 3 of J. Scholtz et al. 2026). Establishing the connection among feedback, cool-gas content, and quenching will therefore require a larger $z \sim 2$ quiescent sample with joint constraints on outflows, molecular gas, and well-measured star-formation histories.

7. CONCLUSION

In this work, we present the largest statistical census to date of Na D-traced neutral interstellar gas and outflows at cosmic noon, based on JWST/NIRSpec medium-resolution spectroscopy of 309 galaxies at $0.6 < z < 4$ drawn from the SMILES, JADES, Blue Jay, and Aurora surveys. Our sample spans a wide range of SFR and M_* , with robust continuum detections in the vicinity of the Na D doublet. By subtracting the stellar photospheric contribution to the Na D doublet, we isolate the neutral ISM component and use it to investigate both the incidence of cool gas absorption and the prevalence and kinematics of neutral outflows across a broad range of galaxy evolutionary stages.

We detect Na D-traced ISM absorption in 76 galaxies, with the vast majority (85%) of detections occurring in massive systems with $\log(M_*/M_\odot) > 10$, whereas lower-mass detections are confined to star-forming galaxies. Our analysis shows that the detectability of Na D absorption depends on different physical factors in different galaxy populations. In star-forming galaxies, Na D strength correlates strongly with dust attenuation, indicating that dust shielding plays a central role in allowing neutral sodium-bearing gas to survive and remain observable. In massive quiescent galaxies, however, dust alone does not explain the presence of Na D. Instead, Na D absorption is preferentially found in both older quiescent systems with larger 4000 Å breaks and younger systems with stronger Balmer absorption $H\delta_A$, consistent with rapid recent quenching. This suggests that, in quiescent galaxies, Na D detectability depends not only on the amount of remaining cool gas, but also on the recent star-formation history.

We further classify the Na D ISM detections according to their kinematics. We identify 26 outflows, 10 inflows, and 36 systems whose Na D absorption is consistent with the systemic velocity. The AGN incidence is higher among galaxies with Na D outflows (46%) than among those with systemic Na D absorption (36%) or inflows

(10%), suggesting that AGN plays an important, though not exclusive, role in driving Na D outflows.

More broadly, our analysis suggests that Na D outflows are driven by different mechanisms in star-forming and quiescent galaxies. In star-forming galaxies, both the incidence and kinematics of neutral outflows correlate with star-formation properties, supporting a predominantly star-formation-driven origin. In quiescent galaxies, by contrast, the outflows show no clear connection to weak residual star formation, and in many cases the energy available from such star formation is insufficient to explain the inferred outflow energetics. Together with the relatively high AGN incidence (63%) among quiescent galaxies hosting Na D outflows, these results suggest that AGN are the primary driver of neutral outflows in quiescent systems at cosmic noon.

However, five quiescent galaxies in our sample with Na D outflows do not show clear evidence for ongoing AGN activity, and the energy output from their residual star formation is too low to account for the observed outflow strengths. We therefore identify these systems as candidates for fossil AGN outflows, in which a past AGN episode may have launched the outflow and the disturbed neutral gas remains observable after the active accretion phase has faded. This scenario remains tentative and will require larger samples and deeper multiwavelength constraints to be tested more directly.

Overall, our results highlight the importance of the cool neutral phase for understanding galaxy quenching at cosmic noon. Substantial neutral gas can persist not only in massive star-forming galaxies but also in quiescent galaxies with distinct quenching histories, while Na D outflows suggest that the processes regulating this gas differ between these populations. Future progress will require larger spectroscopic samples and, ideally, spatially resolved multiphase observations that connect neutral outflows to other gas phases (e.g., ionized and molecular gas), thereby providing a more comprehensive view of the role of feedback and its duty cycle in regulating star formation at cosmic noon.

ACKNOWLEDGMENTS

The authors thank Dr. Sirio Belli and Dr. Weizhe Liu for useful discussions.

This work is based on observations made with the NASA/ESA/CSA James Webb Space Telescope. The JWST data were obtained from the Mikulski Archive for Space Telescopes at the Space Telescope Science Institute, which is operated by the Association of Universities for Research in Astronomy, Inc., under NASA contract NAS 5-03127 for JWST. These observations are associ-

ated with programs 1180, 1181, 1207, 1210, 1286, 1287, 1810, 1837, 1914, and 3215. The authors acknowledge the Blue Jay and Aurora teams for developing their observing programs. A fraction of spectroscopic and photometric data used in this work were retrieved from the Dawn JWST Archive (DJA)¹⁷. DJA is an initiative of the Cosmic Dawn Center (DAWN).

YS, ZJ, YZ, and CNAW acknowledge support from the NIRCcam Science Team contract to the University of Arizona, NAS5-02015. FDE acknowledges support by the Science and Technology Facilities Council (STFC), by the ERC through Advanced Grant 695671 “QUENCH”, and by the UKRI Frontier Research grant RISEandFALL. GHR acknowledges support from the JWST Mid-Infrared Instrument (MIRI) Science Team Lead, grant 80NSSC18K0555, from NASA Goddard Space Flight Center to the University of Arizona. WMB gratefully acknowledges support from DARK via the DARK fellowship and from a research grant (VIL54489) from VILLUM FONDEN. AJB acknowledges funding from the “FirstGalaxies” Advanced Grant from the European Research Council (ERC) under the European Union’s Horizon 2020 research and innovation programme (Grant agreement No. 789056). SC acknowledges support by European Union’s HE ERC Starting Grant No. 101040227 - WINGS. JMH is supported by JWST Program 8544. MP acknowledges support through the grants PID2021-130918NB-I00, PID2024-159902NA-I00, and RYC2023-044853-I, funded by the Spain Ministry of Science and Innovation/State Agency of Research MCIN/AEI/10.13039/501100011033 and El Fondo Social Europeo Plus FSE+. PGP-G acknowledges support from grant PID2022-139567NB-I00 funded by Spanish Ministerio de Ciencia e Innovación MCIN/AEI/10.13039/501100011033, FEDER, UE. HÜ thanks the Max Planck Society for support through the Lise Meitner Excellence Program. HÜ acknowledges funding by the European Union (ERC APEX, 101164796). Views and opinions expressed are however those of the authors only and do not necessarily reflect those of the European Union or the European Research Council Executive Agency. Neither the European Union nor the granting authority can be held responsible for them.

We respectfully acknowledge the University of Arizona is on the land and territories of Indigenous peoples. Today, Arizona is home to 22 federally recognized tribes, with Tucson being home to the O’odham and the Yaqui. The University strives to build sustainable relationships

¹⁷ <https://dawn-cph.github.io/dja/>

Table A1. Properties of galaxies with Na D outflows

1) Survey	2) ID	3) R.A.	4) Decl.	5) z	6) $\log(M_*)$	7) $\log(\text{SFR})$	8) A_V	9) $\text{EW}_{\text{NaD,ISM}}$	10) Δv	11) b
		(deg)	(deg)		(M_\odot)	($M_\odot \text{ yr}^{-1}$)	(mag)	(\AA)	km s^{-1}	km s^{-1}
SMILES	205818	53.197600	-27.786474	1.098	10.57 ^{+0.19} _{-0.72}	1.70 ^{+0.13} _{-0.27}	2.88 ^{+0.23} _{-0.23}	3.39 ^{+1.16} _{-0.96}	-473 ⁺²⁰⁶ ₋₁₆₄	241 ⁺¹¹² ₋₁₅₈
SMILES	206183	53.176590	-27.785521	1.317	11.25 ^{+0.02} _{-0.02}	1.03 ^{+0.02} _{-0.02}	2.27 ^{+0.23} _{-0.23}	9.16 ^{+0.45} _{-0.44}	-440 ⁺⁵⁵ ₋₅₇	273 ⁺⁶⁶ ₋₄₀
SMILES	194473	53.151470	-27.825931	1.612	10.92 ^{+0.05} _{-0.08}	-3.00 ^{+2.35} _{-2.00}	2.12 ^{+0.63} _{-0.63}	3.58 ^{+0.44} _{-0.45}	-168 ⁺¹⁵⁰ ₋₁₆₁	346 ⁺³⁹ ₋₁₁₁
SMILES	201306	53.123138	-27.803460	2.344	11.13 ^{+0.04} _{-0.06}	-3.00 ^{+0.00} _{-0.00}	0.04 ^{+0.04} _{-0.04}	4.08 ^{+0.21} _{-0.21}	-218 ⁺²⁵ ₋₂₅	275 ⁺⁶² ₋₁₀₃
Blue Jay	18668	150.129272	2.369564	2.087	11.20 ^{+0.05} _{-0.05}	-2.70 ^{+1.71} _{-0.30}	4.32 ^{+0.21} _{-0.21}	11.59 ^{+0.73} _{-0.72}	-196 ⁺⁴² ₋₄₆	195 ⁺¹²¹ ₋₁₂₄
Blue Jay	18252	150.098507	2.365359	2.552	11.44 ^{+0.15} _{-0.23}	3.61 ^{+0.16} _{-0.16}	4.37 ^{+0.78} _{-0.78}	9.13 ^{+1.59} _{-1.46}	-326 ⁺⁷⁵ ₋₉₀	118 ⁺¹⁰⁰ ₋₈₀
Blue Jay	11142	150.073292	2.293290	2.445	10.93 ^{+0.20} _{-0.13}	0.26 ^{+0.96} _{-0.49}	0.59 ^{+0.59} _{-0.59}	6.73 ^{+0.33} _{-0.32}	-233 ⁺²² ₋₂₃	90 ⁺⁷⁶ ₋₆₂
Blue Jay	11136	150.109048	2.294328	1.863	10.95 ^{+0.36} _{-0.25}	1.50 ^{+0.49} _{-0.41}	3.58 ^{+1.37} _{-0.67}	5.91 ^{+0.41} _{-0.40}	-139 ⁺²⁷ ₋₂₈	34 ⁺⁴⁰ ₋₂₄
Blue Jay	10339	150.093876	2.284722	2.364	10.50 ^{+0.09} _{-0.12}	-2.15 ^{+1.53} _{-0.54}	0.99 ^{+0.57} _{-0.44}	5.27 ^{+0.37} _{-0.36}	-201 ⁺³⁴ ₋₃₂	126 ⁺⁷⁸ ₋₇₇
Blue Jay	10314	150.085725	2.285124	2.099	11.03 ^{+0.13} _{-0.13}	1.24 ^{+0.31} _{-0.48}	3.57 ^{+0.03} _{-0.03}	2.98 ^{+0.35} _{-0.35}	-154 ⁺⁶⁹ ₋₅₆	144 ⁺⁹² ₋₈₉
Blue Jay	9871	150.077798	2.281137	2.046	11.64 ^{+0.09} _{-0.10}	0.52 ^{+1.19} _{-0.49}	3.57 ^{+0.46} _{-0.46}	9.12 ^{+0.33} _{-0.34}	-209 ⁺²⁷ ₋₂₆	163 ⁺²⁸ ₋₂₉
Blue Jay	8002	150.119934	2.261021	2.687	9.98 ^{+0.16} _{-0.27}	2.19 ^{+0.03} _{-0.04}	2.82 ^{+0.05} _{-0.05}	4.09 ^{+0.43} _{-0.41}	-557 ⁺⁸³ ₋₇₅	209 ⁺⁹⁶ ₋₁₀₀
JADES	42573	53.178703	-27.802702	2.694	10.94 ^{+0.09} _{-0.05}	1.85 ^{+0.15} _{-0.22}	4.27 ^{+0.77} _{-0.57}	8.29 ^{+0.87} _{-0.87}	-138 ⁺¹³³ ₋₁₁₁	73 ⁺¹¹⁰ ₋₅₂
JADES	44571	53.140316	-27.797596	1.768	10.57 ^{+0.04} _{-0.06}	-2.40 ^{+1.60} _{-0.60}	1.23 ^{+0.28} _{-0.42}	3.80 ^{+0.60} _{-0.56}	-160 ⁺⁶⁵ ₋₇₀	104 ⁺¹⁰¹ ₋₇₁
JADES	51236	53.146172	-27.779959	2.582	10.94 ^{+0.24} _{-0.22}	1.88 ^{+0.29} _{-0.36}	5.78 ^{+1.08} _{-1.08}	6.79 ^{+0.56} _{-0.57}	-389 ⁺⁹⁰ ₋₆₁	352 ⁺³⁷ ₋₈₉
JADES	171147	53.055626	-27.874064	2.563	11.35 ^{+0.02} _{-0.02}	-1.85 ^{+1.25} _{-0.54}	0.46 ^{+0.20} _{-0.21}	2.62 ^{+0.24} _{-0.24}	-257 ⁺⁶⁸ ₋₇₀	281 ⁺⁸⁹ ₋₁₄₃
JADES	197911	53.165314	-27.814140	3.064	11.40 ^{+0.08} _{-0.14}	-1.17 ^{+1.19} _{-0.50}	0.10 ^{+0.10} _{-0.10}	2.38 ^{+0.20} _{-0.20}	-389 ⁺⁴⁰ ₋₄₆	192 ⁺⁸⁹ ₋₉₂
JADES	202925	53.163022	-27.797727	1.999	10.52 ^{+0.05} _{-0.05}	-1.55 ^{+1.25} _{-0.49}	1.43 ^{+0.33} _{-0.51}	1.81 ^{+0.44} _{-0.43}	-223 ⁺¹⁴⁹ ₋₁₅₆	156 ⁺¹⁴⁵ ₋₁₀₉
JADES	215262	53.141019	-27.755119	2.131	10.84 ^{+0.10} _{-0.07}	1.75 ^{+0.12} _{-0.13}	1.83 ^{+0.12} _{-0.12}	4.63 ^{+1.88} _{-1.06}	-212 ⁺¹⁸⁷ ₋₃₁₂	226 ⁺¹²¹ ₋₁₅₁
JADES	199773	53.163241	-27.809057	2.821	10.78 ^{+0.09} _{-0.03}	-0.36 ^{+0.19} _{-0.35}	0.45 ^{+0.17} _{-0.36}	4.26 ^{+0.63} _{-0.62}	-128 ⁺⁸² ₋₉₀	112 ⁺¹¹⁷ ₋₇₇
JADES	25055	189.160382	62.227502	1.018	11.33 ^{+0.06} _{-0.39}	-2.70 ^{+1.54} _{-0.30}	0.70 ^{+0.45} _{-0.45}	3.22 ^{+0.31} _{-0.31}	-182 ⁺¹⁴¹ ₋₂₃₉	181 ⁺¹¹² ₋₁₁₂
JADES	29711	189.196910	62.284104	2.320	10.57 ^{+0.18} _{-0.18}	2.51 ^{+0.11} _{-0.30}	5.06 ^{+0.83} _{-0.83}	7.60 ^{+1.34} _{-1.26}	-300 ⁺¹³⁸ ₋₁₁₇	187 ⁺¹³¹ ₋₁₂₇
JADES	33159	189.194706	62.307222	2.050	10.49 ^{+0.15} _{-0.08}	-3.00 ^{+0.00} _{-0.00}	0.72 ^{+0.59} _{-0.43}	2.06 ^{+0.63} _{-0.60}	-261 ⁺²⁵⁰ ₋₂₇₃	255 ⁺¹⁰⁸ ₋₁₅₉
JADES	64818	189.026770	62.289835	1.360	9.46 ^{+0.24} _{-0.33}	1.63 ^{+0.07} _{-0.05}	1.97 ^{+0.07} _{-0.07}	2.98 ^{+1.72} _{-0.95}	-299 ⁺²²⁹ ₋₂₈₅	234 ⁺¹²³ ₋₁₅₈
Aurora	50	150.179276	2.233684	2.294	11.06 ^{+0.08} _{-0.20}	-0.06 ^{+2.47} _{-0.49}	3.79 ^{+0.65} _{-0.65}	7.34 ^{+0.59} _{-0.54}	-290 ⁺⁴⁸ ₋₅₁	117 ⁺⁹⁷ ₋₇₈
Aurora	5901	150.189388	2.238137	2.396	9.67 ^{+0.46} _{-0.35}	1.76 ^{+0.13} _{-0.16}	1.43 ^{+0.10} _{-0.10}	3.26 ^{+1.13} _{-0.90}	-345 ⁺²⁰² ₋₂₁₃	212 ⁺¹²⁵ ₋₁₄₀

NOTE—1) Survey Name; 2) Source NIRSspec ID; 3) and 4) Sky coordinate; 5) pPXF-derived spectroscopic redshift; 6) SED-derived stellar mass; 7) SED-derived SFR within the recent 30 Myr; 8) Dust attenuation; 9) Equivalent width of ISM component of Na D; 10) Velocity offset of Na D ISM component relative to the systemic redshift; 11) Doppler width of the Na D ISM component.

with sovereign Native Nations and Indigenous communities through education offerings, partnerships, and community service.

Facilities: JWST

Software: `AstroPy` (Astropy Collaboration et al. 2013, 2018, 2022), `emcee` (D. Foreman-Mackey et al.

2013), `Prospector` (B. D. Johnson et al. 2021), `SciPy` (P. Virtanen et al. 2020), `pPXF` (M. Cappellari 2017; M. Cappellari 2023)

APPENDIX

A. NA D ISM ABSORPTION DETECTED SAMPLE

In this section, we first present the host galaxy properties and their best-fit Na D profiles of 26 Na D outflows, 10 inflows, and 36 systemic ISMs. The fitting procedure is described in detail in Section 4.2. The profiles of detected outflows, inflows, and systemic ISMs are shown in Figure A1, A2, and A3, respectively, and their

host galaxy properties and best-fit profile parameters are shown in Table A1, A2, and A3, respectively.

Finally, in Table A4, we list the outflow properties (V_{out} , \dot{M}_{out} , \dot{E}_{out} , \dot{p}_{out} , and η), and their host galaxy type and AGN classifications. The definition for each outflow property is described in Section 5.2.1.

Table A2. Properties of galaxies with Na D inflows

1) Survey	2) ID	3) R.A.	4) Decl.	5) z	6) $\log(M_*)$	7) $\log(\text{SFR})$	8) A_V	9) $\text{EW}_{\text{NaD,ISM}}$	10) Δv	11) b
		(deg)	(deg)		(M_\odot)	($M_\odot \text{ yr}^{-1}$)	(mag)	(\AA)	(km s^{-1})	(km s^{-1})
SMILES	199799	53.128826	-27.809018	1.887	$9.95^{+0.08}_{-0.05}$	$0.81^{+0.21}_{-0.25}$	$0.11^{+0.11}_{-0.11}$	$7.94^{+1.22}_{-1.16}$	540^{+41}_{-40}	68^{+62}_{-46}
SMILES	191748	53.101990	-27.834628	2.675	$10.87^{+0.05}_{-0.04}$	$-3.00^{+0.00}_{-0.00}$	$0.63^{+0.34}_{-0.28}$	$2.14^{+0.45}_{-0.42}$	161^{+73}_{-107}	117^{+166}_{-83}
Blue Jay	19572	150.133196	2.378721	1.866	$11.13^{+0.11}_{-0.10}$	$0.14^{+0.71}_{-0.49}$	$3.02^{+0.70}_{-0.75}$	$5.03^{+0.26}_{-0.25}$	150^{+18}_{-19}	27^{+18}_{-19}
Blue Jay	13174	150.112224	2.313952	2.099	$11.27^{+0.19}_{-0.24}$	$2.59^{+0.14}_{-0.30}$	$2.45^{+0.12}_{-0.12}$	$6.37^{+1.86}_{-1.69}$	170^{+137}_{-120}	179^{+119}_{-119}
JADES	192316	53.168046	-27.832569	0.671	$10.34^{+0.11}_{-0.18}$	$-0.75^{+0.27}_{-0.48}$	$0.83^{+0.57}_{-0.36}$	$0.73^{+0.39}_{-0.39}$	371^{+218}_{-283}	177^{+145}_{-122}
JADES	215644	53.214184	-27.753964	1.665	$11.21^{+0.07}_{-0.06}$	$-2.15^{+1.36}_{-0.54}$	$1.02^{+0.42}_{-0.33}$	$2.14^{+0.42}_{-0.40}$	140^{+94}_{-90}	269^{+75}_{-77}
JADES	10008071	53.154460	-27.771433	2.227	$9.34^{+0.15}_{-0.09}$	$1.61^{+0.02}_{-0.05}$	$0.85^{+0.10}_{-0.10}$	$8.24^{+2.42}_{-2.50}$	352^{+116}_{-114}	138^{+139}_{-95}
JADES	25351	189.173371	62.230410	3.128	$9.75^{+0.13}_{-0.18}$	$1.66^{+0.11}_{-0.17}$	$1.86^{+0.09}_{-0.09}$	$5.11^{+1.84}_{-1.73}$	260^{+149}_{-170}	162^{+140}_{-111}
JADES	30960	189.174713	62.249076	0.850	$10.72^{+0.12}_{-0.08}$	$0.55^{+0.31}_{-0.39}$	$1.97^{+0.77}_{-0.77}$	$4.05^{+1.37}_{-1.30}$	248^{+336}_{-150}	175^{+181}_{-126}
JADES	30817	189.197539	62.291329	2.244	$9.79^{+0.09}_{-0.08}$	$1.67^{+0.06}_{-0.06}$	$1.59^{+0.05}_{-0.05}$	$2.90^{+0.82}_{-0.78}$	183^{+106}_{-89}	96^{+116}_{-67}

NOTE—1)-11) Same as Table A1.

B. SED-DERIVED AND $H\alpha$ -DERIVED SFR COMPARISON

In this section, we test the robustness of our SFR estimation through SED modeling (Section 4.4) by comparing it with $H\alpha$ -inferred SFR. As we mentioned in Section 4.1 $H\alpha$ flux and uncertainty are estimated from pPXF stellar+nebular emission modeling using Monte Carlo, and then dust-corrected using A_V derived from the Balmer Decrement, or SED if Balmer Decrement is unavailable. Furthermore, as we pointed out in Section 2, we correct the slit-loss of the MSA spectrum by matching with the broad-band NIRCcam photometries for individual galaxies to derive the total $H\alpha$ luminosity of the entire galaxy. Finally, to ensure reliable $H\alpha$ -based SFR, we exclude the galaxies with low-SNR $H\alpha$ ($\text{SNR} < 1$) or classified as AGN or lie in the “composite” region of the [N II]-BPT diagram (see Section 5.1.4). Finally, we convert $L_{H\alpha}$ to SFR using the relation from R. C. Kennicutt & N. J. Evans (2012).

Figure B1 illustrates the comparison between SED-based and $H\alpha$ -based SFR for the parent galaxies with reliable $H\alpha$ -based SFR measurements. Overall, the two estimates agree well, with increasing scatter and larger SED uncertainties toward low SFR $\log(\text{SFR}_{\text{SED}}[M_\odot \text{ yr}^{-1}]) < 0$, supporting the robustness of our SED modeling.

One notable outlier lies in the lower right corner of Figure B1, whose SED-based SFR is much smaller than the $H\alpha$ -based one. This galaxy is SMILES-207739 ($z = 1.04$), a faint submillimeter galaxy with ALMA detection by the ASPECS-LP program (M. Aravena et al. 2020). Using multiwavelength photometry from the optical to millimeter, M. Aravena et al. (2020) derived its SED-based SFR with $\log(\text{SFR}[M_\odot \text{ yr}^{-1}]) = 1.25$, 4 dex higher than our SED-derived SFR. Adopting their

IR/mm-constrained SED-based SFR reduces the discrepancy, bringing the SED- and $H\alpha$ -based SFRs into agreement within the overall scatter (~ 1 dex difference). This suggests that for SMILES-207739, despite its general low SFR ($\log(\text{sSFR}[\text{yr}^{-1}]) \sim -10$), our UV-to-NIR SED fitting underestimates its true SFR because it lacks the mid/far-IR and mm constraints which can robustly capture heavily obscured star formation.

C. COMPARISON BETWEEN THREE-NOD VERSUS TWO-NOD LOCAL BACKGROUND SUBTRACTION

We assess the potential self-subtraction problem when using the three-nod background subtraction for spatially extended galaxies. As a representative case, we select JADES-25055 at $z = 1.018$, which has an effective radius of $r_e = 0.44''$ (Figure C1, left). The middle panel of Figure C1 compares the spectrum adopted in this work, which is reduced with the three-nod local background subtraction, to the alternative two-nod reduction. We find that the spectra between the three-nod and two-nod versions are broadly consistent, although the three-nod spectrum shows a slightly shallower Na D absorption (most noticeably on the blue side), which may be due to modest self-subtraction in the local-background estimate for an extended source.

We further quantify the impact on the derived interstellar Na D equivalent width $\text{EW}_{\text{NaD,ISM}}$, and outflow velocity V_{out} . As shown in the right panel of Figure C1, the values measured from the two-nod spectrum are slightly larger than those from the three-nod spectrum, consistent with the deeper and bluer Na D profile in the former. However, the differences are $< 20\%$ and fully consistent within the 1σ uncertainties of our fiducial (three-nod) measurements. We therefore conclude

Table A3. Properties of galaxies with Na D systemic ISM

1) Survey	2) ID	3) R.A. (deg)	4) Decl. (deg)	5) z	6) $\log(M_*)$ (M_\odot)	7) $\log(\text{SFR})$ ($M_\odot \text{ yr}^{-1}$)	8) A_V (mag)	9) $\text{EW}_{\text{NaD,ISM}}$ (Å)	10) Δv (km s^{-1})	11) b (km s^{-1})
SMILES	209480	53.149098	-27.774387	1.093	10.92 ^{+0.14} _{-0.08}	-1.20 ^{+1.73} _{-0.50}	1.40 ^{+0.49} _{-0.49}	2.56 ^{+0.62} _{-0.64}	-29 ⁺⁹³ ₋₈₇	106 ⁺¹⁰¹ ₋₇₃
SMILES	212434	53.151409	-27.766742	0.895	9.61 ^{+0.23} _{-0.20}	1.11 ^{+0.10} _{-0.12}	2.75 ^{+0.40} _{-0.51}	2.75 ^{+0.79} _{-0.77}	-10 ⁺⁸⁰ ₋₆₃	90 ⁺¹¹² ₋₆₃
SMILES	214075	53.196909	-27.760532	3.603	10.65 ^{+0.12} _{-0.06}	-0.53 ^{+1.27} _{-0.50}	1.47 ^{+0.67} _{-0.42}	6.38 ^{+0.77} _{-0.74}	-4 ⁺⁵¹ ₋₄₉	123 ⁺⁹⁵ ₋₇₈
SMILES	207739	53.179110	-27.780619	1.038	11.25 ^{+0.03} _{-0.03}	-3.00 ^{+0.00} _{-0.00}	5.58 ^{+0.41} _{-0.41}	10.23 ^{+0.92} _{-0.91}	-56 ⁺²⁹ ₋₂₉	53 ⁺⁵³ ₋₃₇
SMILES	198545	53.161414	-27.811144	2.827	11.13 ^{+0.03} _{-0.05}	0.59 ^{+0.09} _{-0.09}	3.67 ^{+0.44} _{-0.44}	9.23 ^{+1.04} _{-1.04}	-4 ⁺²⁸ ₋₂₈	37 ⁺⁴¹ ₋₂₆
SMILES	201027	53.126930	-27.804682	2.870	10.71 ^{+0.03} _{-0.44}	-0.49 ^{+1.86} _{-0.50}	1.93 ^{+0.45} _{-0.50}	7.31 ^{+0.84} _{-0.80}	-6 ⁺⁴⁹ ₋₄₇	69 ⁺⁷⁶ ₋₄₈
SMILES	204520	53.125113	-27.790849	1.551	11.26 ^{+0.08} _{-0.06}	0.44 ^{+0.44} _{-0.44}	2.83 ^{+0.82} _{-0.82}	1.84 ^{+0.31} _{-0.30}	-11 ⁺⁵⁸ ₋₆₀	146 ⁺¹¹¹ ₋₈₉
Blue Jay	11494	150.073883	2.297977	2.093	11.70 ^{+0.06} _{-0.05}	-2.15 ^{+1.49} _{-0.54}	0.69 ^{+0.32} _{-0.27}	3.72 ^{+1.79} _{-0.34}	-269 ⁺⁴⁰⁸ ₋₂₂	30 ⁺³⁶⁶ ₋₂₂
Blue Jay	10565	150.094200	2.287267	2.441	10.78 ^{+0.20} _{-0.23}	-0.05 ^{+1.21} _{-0.50}	0.66 ^{+0.66} _{-0.66}	3.23 ^{+0.59} _{-0.54}	84 ⁺⁶⁸ ₋₁₀₃	121 ⁺¹²³ ₋₈₆
Blue Jay	10021	150.089377	2.282296	1.811	10.08 ^{+0.17} _{-0.17}	0.53 ^{+0.49} _{-0.46}	2.22 ^{+0.79} _{-0.51}	6.81 ^{+1.58} _{-1.91}	-414 ⁺⁵²¹ ₋₁₆₄	383 ⁺¹⁴ ₋₉₀
Blue Jay	19705	150.107752	2.379484	2.467	11.33 ^{+0.10} _{-0.22}	-0.87 ^{+1.47} _{-0.49}	5.68 ^{+1.17} _{-1.34}	7.25 ^{+1.40} _{-1.41}	-79 ⁺⁸⁶ ₋₁₀₀	153 ⁺¹⁴¹ ₋₁₀₈
Blue Jay	18071	150.135268	2.363612	2.822	10.45 ^{+0.45} _{-0.30}	1.91 ^{+0.25} _{-0.30}	2.53 ^{+0.03} _{-0.03}	2.20 ^{+0.77} _{-0.79}	-115 ⁺¹²⁸ ₋₁₄₄	125 ⁺⁹⁰ ₋₉₀
Blue Jay	16419	150.095610	2.350069	1.925	11.34 ^{+0.09} _{-0.10}	0.87 ^{+0.57} _{-0.48}	0.59 ^{+0.35} _{-0.35}	1.79 ^{+0.33} _{-0.34}	-243 ⁺²⁵⁵ ₋₁₄₃	366 ⁺²⁷ ₋₁₀₁
Blue Jay	10245	150.089814	2.284797	1.808	10.55 ^{+0.19} _{-0.27}	2.17 ^{+0.11} _{-0.35}	2.49 ^{+0.73} _{-0.68}	2.76 ^{+0.37} _{-0.35}	14 ⁺³⁴ ₋₃₃	46 ⁺⁴⁹ ₋₃₂
Blue Jay	9395	150.125656	2.275250	2.127	10.78 ^{+0.04} _{-0.04}	-2.40 ^{+1.74} _{-0.60}	0.77 ^{+0.55} _{-0.39}	1.80 ^{+0.37} _{-0.36}	-60 ⁺¹⁸¹ ₋₁₁₅	218 ⁺¹³² ₋₁₄₆
Blue Jay	9180	150.135692	2.272714	1.603	10.58 ^{+0.29} _{-0.38}	1.50 ^{+0.37} _{-0.49}	2.93 ^{+0.11} _{-0.11}	6.70 ^{+0.66} _{-0.59}	-54 ⁺⁶⁰ ₋₇₂	118 ⁺⁶⁹ ₋₇₅
JADES	8375	53.144518	-27.779103	1.551	10.25 ^{+0.10} _{-0.10}	1.21 ^{+0.09} _{-0.07}	2.67 ^{+0.32} _{-0.32}	5.39 ^{+2.73} _{-2.68}	-256 ⁺²⁶⁷ ₋₂₃₄	199 ⁺¹⁴⁰ ₋₁₃₉
JADES	44832	53.132648	-27.732383	1.548	10.43 ^{+0.29} _{-0.22}	1.90 ^{+0.32} _{-0.29}	2.53 ^{+0.18} _{-0.18}	3.62 ^{+0.80} _{-0.77}	-103 ⁺¹²⁰ ₋₉₂	90 ⁺¹¹³ ₋₆₃
JADES	34145	189.121246	62.314985	1.778	10.80 ^{+0.13} _{-0.11}	-1.07 ^{+1.60} _{-0.50}	2.44 ^{+0.80} _{-0.86}	2.86 ^{+1.06} _{-1.14}	-103 ⁺¹³⁸ ₋₁₃₂	78 ⁺¹⁰⁰ ₋₅₅
JADES	138717	53.119187	-27.765842	1.884	10.60 ^{+0.12} _{-0.07}	-2.52 ^{+1.51} _{-0.48}	1.58 ^{+0.54} _{-0.50}	5.41 ^{+0.30} _{-0.29}	31 ⁺¹⁷ ₋₁₇	86 ⁺⁴² ₋₅₀
JADES	163028	53.099629	-27.890669	1.588	11.25 ^{+0.01} _{-0.01}	1.62 ^{+0.04} _{-0.04}	3.92 ^{+0.28} _{-0.31}	1.38 ^{+0.37} _{-0.36}	-48 ⁺¹⁶⁷ ₋₂₈₉	332 ⁺⁵³ ₋₁₁₅
JADES	173387	53.109875	-27.870195	2.697	10.14 ^{+0.09} _{-0.09}	0.65 ^{+0.46} _{-0.48}	2.05 ^{+0.06} _{-0.06}	0.80 ^{+0.64} _{-0.56}	120 ⁺¹⁶⁸ ₋₂₅₈	121 ⁺¹⁵¹ ₋₈₆
JADES	180575	53.085472	-27.858170	3.473	10.93 ^{+0.10} _{-0.19}	2.97 ^{+0.11} _{-0.11}	2.35 ^{+0.10} _{-0.10}	4.16 ^{+2.27} _{-2.21}	-106 ⁺¹⁸⁸ ₋₂₈₂	164 ⁺¹⁴² ₋₁₁₂
JADES	189524	53.131446	-27.841383	1.614	11.50 ^{+0.22} _{-0.04}	0.79 ^{+0.54} _{-0.48}	4.23 ^{+1.41} _{-0.77}	8.44 ^{+0.88} _{-0.88}	37 ⁺⁵³ ₋₅₆	292 ⁺⁷² ₋₁₀₂
JADES	10031863	53.116127	-27.841503	2.035	10.45 ^{+0.23} _{-0.09}	1.13 ^{+0.16} _{-0.16}	1.67 ^{+0.14} _{-0.14}	4.42 ^{+1.34} _{-1.39}	14 ⁺¹⁴⁵ ₋₁₁₁	124 ⁺¹⁴⁶ ₋₈₇
JADES	22456	189.035722	62.243154	3.129	10.91 ^{+0.19} _{-0.34}	2.83 ^{+0.16} _{-0.23}	4.40 ^{+0.69} _{-0.69}	6.32 ^{+2.25} _{-1.90}	14 ⁺²²⁶ ₋₁₄₇	188 ⁺¹⁴⁰ ₋₁₄₀
JADES	28428	189.235679	62.253620	2.953	11.23 ^{+0.05} _{-0.09}	0.15 ^{+0.76} _{-0.48}	4.90 ^{+0.60} _{-0.71}	7.75 ^{+1.90} _{-1.82}	47 ⁺¹³⁵ ₋₁₅₂	289 ⁺⁸¹ ₋₁₃₇
JADES	29715	189.091535	62.283901	1.879	9.52 ^{+0.26} _{-0.10}	0.89 ^{+0.09} _{-0.13}	1.32 ^{+0.14} _{-0.14}	3.83 ^{+1.40} _{-1.28}	104 ⁺¹⁵⁰ ₋₁₂₂	151 ⁺¹³⁷ ₋₁₀₁
JADES	64734	189.021773	62.296589	1.382	9.89 ^{+0.15} _{-0.07}	0.80 ^{+0.08} _{-0.13}	1.05 ^{+0.92} _{-0.92}	0.67 ^{+0.63} _{-0.47}	-2 ⁺³³⁰ ₋₂₃₁	149 ⁺¹⁴⁶ ₋₁₀₅
JADES	71914	189.253780	62.167011	2.459	9.84 ^{+0.46} _{-0.26}	0.93 ^{+0.58} _{-0.38}	2.42 ^{+0.91} _{-1.00}	6.60 ^{+2.55} _{-2.50}	-15 ⁺²⁰⁸ ₋₁₅₈	134 ⁺¹⁶² ₋₉₆
JADES	72396	189.263048	62.170385	2.761	10.84 ^{+0.04} _{-0.08}	-2.05 ^{+1.45} _{-0.65}	1.11 ^{+0.42} _{-0.34}	4.15 ^{+0.97} _{-0.93}	50 ⁺⁸⁷ ₋₉₁	99 ⁺¹²³ ₋₆₉
JADES	72719	189.199697	62.172290	1.736	10.79 ^{+0.09} _{-0.22}	-3.00 ^{+0.00} _{-0.00}	2.96 ^{+1.05} _{-1.05}	4.28 ^{+1.25} _{-1.28}	31 ⁺⁸⁴ ₋₉₁	71 ⁺⁹⁵ ₋₅₀
Aurora	100231	189.224830	62.251141	2.957	10.85 ^{+0.09} _{-0.09}	-0.56 ^{+1.03} _{-0.49}	2.18 ^{+0.23} _{-0.23}	4.96 ^{+1.24} _{-0.71}	-70 ⁺⁶⁴ ₋₁₃₅	210 ⁺¹³² ₋₁₅₄
Aurora	30564	189.204075	62.294341	2.482	10.85 ^{+0.14} _{-0.22}	2.17 ^{+0.18} _{-0.02}	1.69 ^{+0.02} _{-0.02}	1.91 ^{+0.92} _{-0.52}	-194 ⁺²²² ₋₃₇₄	240 ⁺¹¹¹ ₋₁₇₀
Aurora	37	150.181709	2.239991	3.459	10.65 ^{+0.06} _{-0.09}	2.05 ^{+0.20} _{-0.08}	1.53 ^{+0.15} _{-0.15}	2.69 ^{+1.64} _{-1.53}	139 ⁺²¹² ₋₃₂₉	155 ⁺¹⁵⁶ ₋₁₁₀
Aurora	100238	189.178228	62.285188	2.487	11.03 ^{+0.07} _{-0.07}	-2.70 ^{+1.85} _{-1.30}	0.92 ^{+0.55} _{-0.29}	3.42 ^{+0.64} _{-0.59}	42 ⁺⁸⁴ ₋₈₇	213 ⁺¹¹¹ ₋₁₁₇

NOTE—1)-11) Same as Table A1.

that potential self-subtraction in the three-nod reduc-

tion does not significantly affect our Na D measurements and our scientific conclusions.

REFERENCES

- Adscheid, S., Magnelli, B., Liu, D., et al. 2024, *A&A*, 685, A1, doi: [10.1051/0004-6361/202348407](https://doi.org/10.1051/0004-6361/202348407)
- Alberts, S., Lyu, J., Shivaeei, I., et al. 2024, *ApJ*, 976, 224, doi: [10.3847/1538-4357/ad7396](https://doi.org/10.3847/1538-4357/ad7396)
- Aravena, M., Boogaard, L., González-López, J., et al. 2020, *ApJ*, 901, 79, doi: [10.3847/1538-4357/ab99a2](https://doi.org/10.3847/1538-4357/ab99a2)

- Astropy Collaboration, Robitaille, T. P., Tollerud, E. J., et al. 2013, *A&A*, 558, A33, doi: [10.1051/0004-6361/201322068](https://doi.org/10.1051/0004-6361/201322068)
- Astropy Collaboration, Price-Whelan, A. M., Sipőcz, B. M., et al. 2018, *AJ*, 156, 123, doi: [10.3847/1538-3881/aabc4f](https://doi.org/10.3847/1538-3881/aabc4f)
- Astropy Collaboration, Price-Whelan, A. M., Lim, P. L., et al. 2022, *ApJ*, 935, 167, doi: [10.3847/1538-4357/ac7c74](https://doi.org/10.3847/1538-4357/ac7c74)

Table A4. Na D outflow properties

1) Survey	2) ID	3) $\log(V_{\text{out}})$	4) $\log(\dot{M}_{\text{out}})$	5) $\log(\dot{E}_{\text{out}})$	6) $\log(\dot{p}_{\text{out}})$	7) η	8) Class	9) AGN
		$km\ s^{-1}$	$(M_{\odot}\ yr^{-1})$	$(erg\ s^{-1})$	$(dyne)$			
SMILES	205818	$2.90^{+0.13}_{-0.16}$	$1.90^{+0.56}_{-0.78}$	$43.19^{+0.80}_{-1.26}$	$35.59^{+0.68}_{-1.01}$	$0.21^{+0.63}_{-0.79}$	SF	0
SMILES	206183	$2.92^{+0.03}_{-0.03}$	$2.44^{+0.12}_{-0.19}$	$43.77^{+0.14}_{-0.18}$	$36.16^{+0.13}_{-0.18}$	$1.41^{+0.12}_{-0.19}$	QG	0
SMILES	194473	$2.81^{+0.11}_{-0.15}$	$1.93^{+0.34}_{-0.53}$	$43.03^{+0.57}_{-0.92}$	$35.52^{+0.46}_{-0.71}$	$4.93^{+4.34}_{-2.41}$	QG	1
SMILES	201306	$2.78^{+0.07}_{-0.09}$	$1.49^{+0.08}_{-0.10}$	$42.53^{+0.20}_{-0.27}$	$35.06^{+0.14}_{-0.17}$	$4.49^{+0.08}_{-0.10}$	QG	1
Blue Jay	18668	$2.68^{+0.15}_{-0.15}$	$1.98^{+0.19}_{-0.38}$	$42.85^{+0.43}_{-0.84}$	$35.47^{+0.30}_{-0.62}$	$4.68^{+0.28}_{-1.75}$	QG	1
Blue Jay	18252	$2.70^{+0.11}_{-0.10}$	$1.85^{+0.34}_{-0.55}$	$42.76^{+0.51}_{-0.76}$	$35.36^{+0.41}_{-0.66}$	$-1.75^{+0.37}_{-0.57}$	SF	0
Blue Jay	11142	$2.56^{+0.11}_{-0.09}$	$1.22^{+0.27}_{-0.55}$	$41.84^{+0.48}_{-0.77}$	$34.58^{+0.37}_{-0.66}$	$0.96^{+0.52}_{-1.10}$	QG	1
Blue Jay	11136	$2.28^{+0.11}_{-0.09}$	$0.81^{+0.36}_{-0.59}$	$40.87^{+0.58}_{-0.79}$	$33.89^{+0.47}_{-0.69}$	$-0.69^{+0.53}_{-0.77}$	SF	0
Blue Jay	10339	$2.58^{+0.11}_{-0.11}$	$1.16^{+0.26}_{-0.50}$	$41.82^{+0.47}_{-0.79}$	$34.54^{+0.36}_{-0.65}$	$3.31^{+0.55}_{-1.61}$	QG	0
Blue Jay	10314	$2.54^{+0.11}_{-0.10}$	$1.08^{+0.27}_{-0.36}$	$41.70^{+0.44}_{-0.65}$	$34.45^{+0.36}_{-0.51}$	$-0.16^{+0.50}_{-0.48}$	QG	0
Blue Jay	9871	$2.64^{+0.04}_{-0.04}$	$1.79^{+0.07}_{-0.07}$	$42.57^{+0.12}_{-0.13}$	$35.23^{+0.09}_{-0.10}$	$1.26^{+0.32}_{-1.19}$	QG	0
Blue Jay	8002	$2.94^{+0.05}_{-0.09}$	$1.88^{+0.30}_{-0.38}$	$43.30^{+0.32}_{-0.61}$	$35.64^{+0.31}_{-0.48}$	$-0.30^{+0.31}_{-0.38}$	SF	0
JADES	42573	$2.41^{+0.21}_{-0.17}$	$1.19^{+0.50}_{-0.73}$	$41.49^{+0.88}_{-1.23}$	$34.39^{+0.69}_{-0.98}$	$-0.66^{+0.55}_{-0.75}$	SF	1
JADES	44571	$2.49^{+0.19}_{-0.14}$	$1.22^{+0.40}_{-0.63}$	$41.71^{+0.75}_{-1.08}$	$34.52^{+0.57}_{-0.86}$	$3.62^{+0.77}_{-1.72}$	QG	1
JADES	51236	$2.93^{+0.04}_{-0.06}$	$2.02^{+0.25}_{-0.16}$	$43.40^{+0.20}_{-0.21}$	$35.76^{+0.22}_{-0.18}$	$0.14^{+0.38}_{-0.33}$	SF	1
JADES	171147	$2.81^{+0.08}_{-0.11}$	$1.38^{+0.22}_{-0.26}$	$42.52^{+0.27}_{-0.51}$	$35.00^{+0.23}_{-0.38}$	$3.23^{+0.51}_{-1.28}$	QG	0
JADES	197911	$2.82^{+0.08}_{-0.08}$	$1.21^{+0.18}_{-0.26}$	$42.36^{+0.31}_{-0.45}$	$34.84^{+0.24}_{-0.35}$	$2.38^{+0.43}_{-1.22}$	QG	1
JADES	202925	$2.65^{+0.19}_{-0.16}$	$0.92^{+0.51}_{-0.74}$	$41.71^{+0.82}_{-1.23}$	$34.36^{+0.65}_{-0.98}$	$2.47^{+0.75}_{-1.45}$	QG	1
JADES	215262	$2.70^{+0.27}_{-0.19}$	$1.63^{+0.74}_{-0.80}$	$42.48^{+1.31}_{-1.42}$	$35.10^{+1.03}_{-1.10}$	$-0.12^{+0.75}_{-0.81}$	SF	1
JADES	199773	$2.47^{+0.21}_{-0.17}$	$1.12^{+0.46}_{-0.76}$	$41.56^{+0.84}_{-1.34}$	$34.39^{+0.65}_{-1.05}$	$1.48^{+0.58}_{-0.78}$	QG	1
JADES	25055	$2.68^{+0.17}_{-0.16}$	$1.22^{+0.25}_{-0.46}$	$42.06^{+0.54}_{-0.89}$	$34.69^{+0.39}_{-0.67}$	$3.91^{+0.35}_{-1.61}$	QG	1
JADES	29711	$2.75^{+0.11}_{-0.11}$	$1.88^{+0.38}_{-0.55}$	$42.90^{+0.50}_{-0.85}$	$35.44^{+0.43}_{-0.70}$	$-0.63^{+0.47}_{-0.56}$	SF	0
JADES	33159	$2.77^{+0.20}_{-0.18}$	$1.40^{+0.56}_{-0.80}$	$42.44^{+0.88}_{-1.41}$	$34.97^{+0.71}_{-1.10}$	$4.40^{+0.56}_{-0.80}$	QG	0
JADES	64818	$2.78^{+0.23}_{-0.20}$	$1.53^{+0.79}_{-0.88}$	$42.56^{+1.26}_{-1.60}$	$35.09^{+1.03}_{-1.23}$	$-0.11^{+0.79}_{-0.88}$	SF	0
Aurora	50	$2.66^{+0.11}_{-0.10}$	$1.66^{+0.25}_{-0.47}$	$42.50^{+0.44}_{-0.74}$	$35.13^{+0.34}_{-0.60}$	$1.71^{+0.49}_{-2.52}$	QG	1
Aurora	5901	$2.81^{+0.16}_{-0.16}$	$1.59^{+0.55}_{-0.77}$	$42.68^{+0.84}_{-1.24}$	$35.19^{+0.69}_{-1.00}$	$-0.16^{+0.57}_{-0.78}$	SF	0

NOTE—1) Survey Name; 2) Source NIRSpc ID; 3) Outflow Velocity, defined as $\Delta v + 2\sigma$; 4) Outflow Mass rate; 5) Outflow energy rate; 6) Outflow momentum rate; 7) mass loading factor, defined as $\dot{M}_{\text{out}}/\text{SFR}$; 8) Host galaxy type: “SF” and “QG” means star-forming and quiescent, respectively; 9) 1 (0) if host has (does not have) an AGN.

- Avery, C. R., Wuyts, S., Förster Schreiber, N. M., et al. 2022, MNRAS, 511, 4223, doi: [10.1093/mnras/stac190](https://doi.org/10.1093/mnras/stac190)
- Baker, W. M., Valentino, F., Lagos, C. d. P., et al. 2025a, A&A, 702, A270, doi: [10.1051/0004-6361/202555829](https://doi.org/10.1051/0004-6361/202555829)
- Baker, W. M., Lim, S., D’Eugenio, F., et al. 2025b, MNRAS, 539, 557, doi: [10.1093/mnras/staf475](https://doi.org/10.1093/mnras/staf475)
- Baldwin, J. A., Phillips, M. M., & Terlevich, R. 1981, PASP, 93, 5, doi: [10.1086/130766](https://doi.org/10.1086/130766)
- Balogh, M. L., Morris, S. L., Yee, H. K. C., Carlberg, R. G., & Ellingson, E. 1999, ApJ, 527, 54, doi: [10.1086/308056](https://doi.org/10.1086/308056)
- Baron, D., Netzer, H., Lutz, D., Prochaska, J. X., & Davies, R. I. 2022, MNRAS, 509, 4457, doi: [10.1093/mnras/stab3232](https://doi.org/10.1093/mnras/stab3232)
- Belli, S., Park, M., Davies, R. L., et al. 2024, Nature, 630, 54, doi: [10.1038/s41586-024-07412-1](https://doi.org/10.1038/s41586-024-07412-1)
- Belli, S., Bugiani, L., Park, M., et al. 2025, arXiv e-prints, arXiv:2510.11775, doi: [10.48550/arXiv.2510.11775](https://doi.org/10.48550/arXiv.2510.11775)
- Bezanson, R., Spilker, J. S., Suess, K. A., et al. 2022, ApJ, 925, 153, doi: [10.3847/1538-4357/ac3dfa](https://doi.org/10.3847/1538-4357/ac3dfa)
- Brinchmann, J., Charlot, S., White, S. D. M., et al. 2004, MNRAS, 351, 1151, doi: [10.1111/j.1365-2966.2004.07881.x](https://doi.org/10.1111/j.1365-2966.2004.07881.x)
- Bugiani, L., Belli, S., Park, M., et al. 2025, ApJ, 981, 25, doi: [10.3847/1538-4357/adaeaf](https://doi.org/10.3847/1538-4357/adaeaf)
- Bunker, A. J., Cameron, A. J., Curtis-Lake, E., et al. 2024, A&A, 690, A288, doi: [10.1051/0004-6361/202347094](https://doi.org/10.1051/0004-6361/202347094)
- Byler, N., Dalcanton, J. J., Conroy, C., & Johnson, B. D. 2017, ApJ, 840, 44, doi: [10.3847/1538-4357/aa6c66](https://doi.org/10.3847/1538-4357/aa6c66)
- Calzetti, D., Armus, L., Bohlin, R. C., et al. 2000, ApJ, 533, 682, doi: [10.1086/308692](https://doi.org/10.1086/308692)
- Cappellari, M. 2017, MNRAS, 466, 798, doi: [10.1093/mnras/stw3020](https://doi.org/10.1093/mnras/stw3020)
- Cappellari, M. 2023, MNRAS, 526, 3273, doi: [10.1093/mnras/stad2597](https://doi.org/10.1093/mnras/stad2597)
- Cappellari, M., & Emsellem, E. 2004, PASP, 116, 138, doi: [10.1086/381875](https://doi.org/10.1086/381875)
- Carnall, A. C., McLure, R. J., Dunlop, J. S., & Davé, R. 2018, MNRAS, 480, 4379, doi: [10.1093/mnras/sty2169](https://doi.org/10.1093/mnras/sty2169)

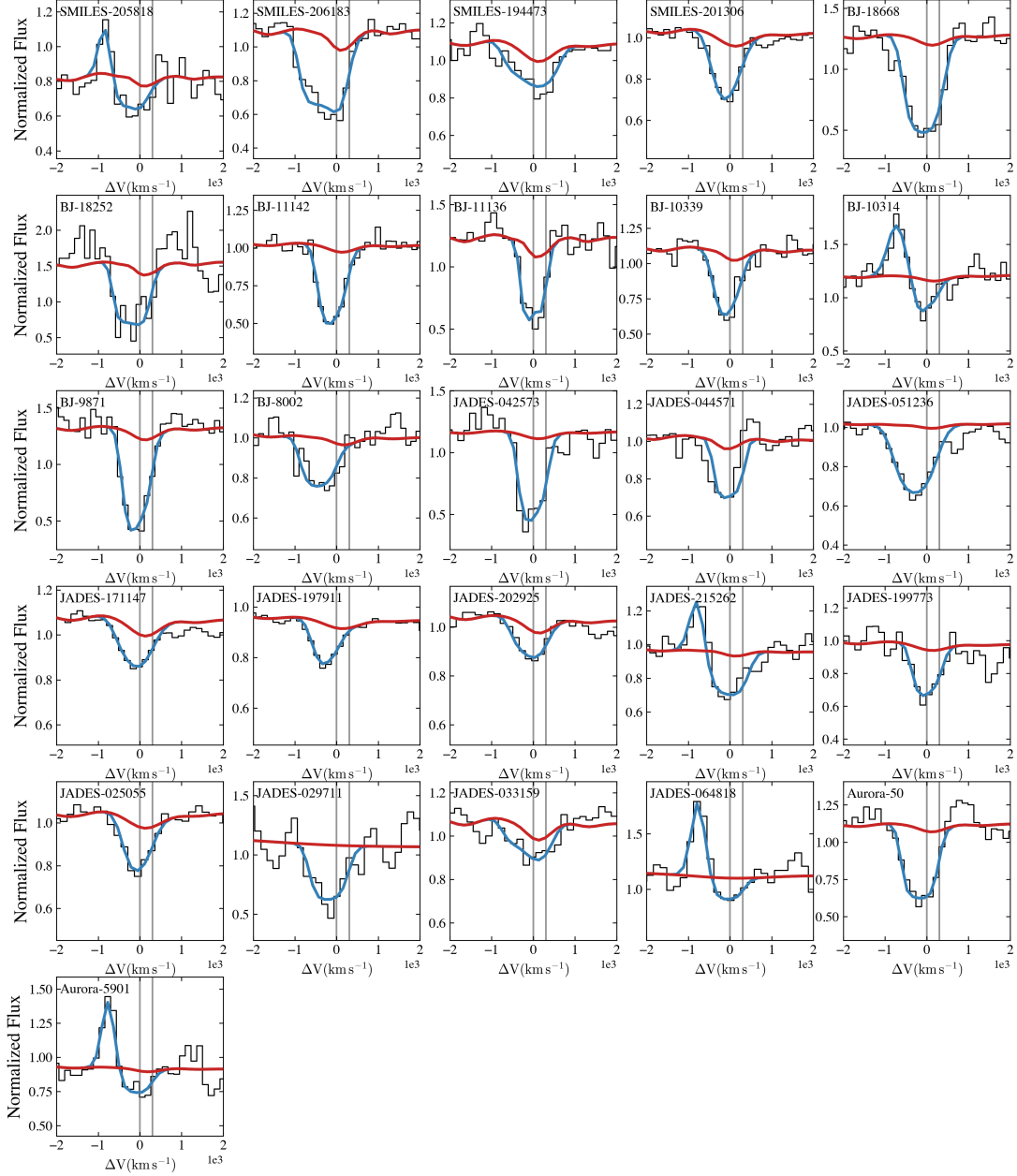


Figure A1. Best-fit Na D profile of 26 outflows. The black, red, and blue lines show the 1D JWST/NIRSpec MSA spectrum, the best-fit stellar continuum by pPXF, and the best-fit ISM Na D absorption (+ He I 5877 Å emission if present), respectively. The two gray vertical lines illustrate the systemic velocity of Na D $\lambda\lambda$ 5890, 5896.

Cazzoli, S., Arribas, S., Maiolino, R., & Colina, L. 2016,

A&A, 590, A125, doi: [10.1051/0004-6361/201526788](https://doi.org/10.1051/0004-6361/201526788)

Chen, Y.-M., Tremonti, C. A., Heckman, T. M., et al. 2010,

AJ, 140, 445, doi: [10.1088/0004-6256/140/2/445](https://doi.org/10.1088/0004-6256/140/2/445)

Choi, J., Dotter, A., Conroy, C., et al. 2016, ApJ, 823, 102,

doi: [10.3847/0004-637X/823/2/102](https://doi.org/10.3847/0004-637X/823/2/102)

Coil, A. L., Weiner, B. J., Holz, D. E., et al. 2011, ApJ,

743, 46, doi: [10.1088/0004-637X/743/1/46](https://doi.org/10.1088/0004-637X/743/1/46)

Concas, A., Popesso, P., Brusa, M., et al. 2017, A&A, 606,

A36, doi: [10.1051/0004-6361/201629519](https://doi.org/10.1051/0004-6361/201629519)

Concas, A., Popesso, P., Brusa, M., Mainieri, V., &

Thomas, D. 2019, A&A, 622, A188,

doi: [10.1051/0004-6361/201732152](https://doi.org/10.1051/0004-6361/201732152)

Conroy, C., & Gunn, J. E. 2010, ApJ, 712, 833,

doi: [10.1088/0004-637X/712/2/833](https://doi.org/10.1088/0004-637X/712/2/833)

Conroy, C., Gunn, J. E., & White, M. 2009, ApJ, 699, 486,

doi: [10.1088/0004-637X/699/1/486](https://doi.org/10.1088/0004-637X/699/1/486)

Cowie, L. L., Barger, A. J., Hsu, L.-Y., et al. 2017, ApJ,

837, 139, doi: [10.3847/1538-4357/aa60bb](https://doi.org/10.3847/1538-4357/aa60bb)

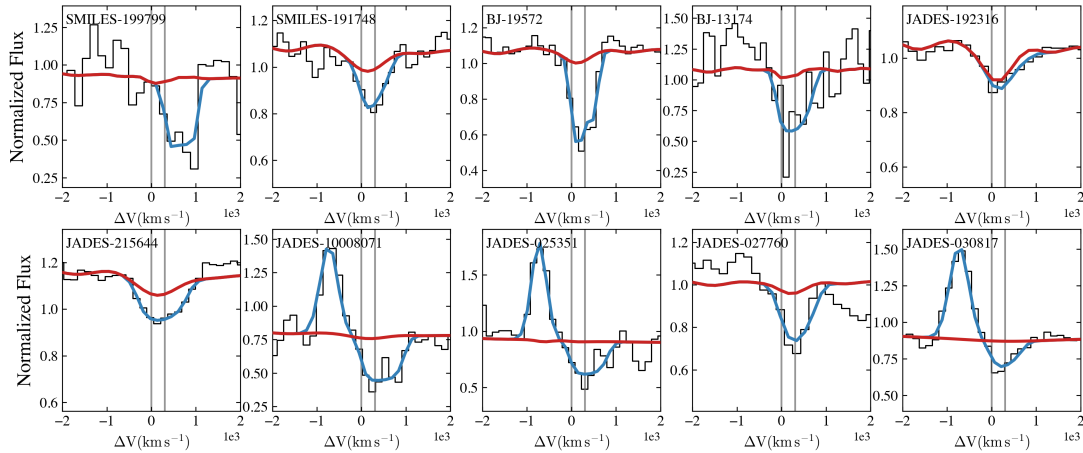


Figure A2. Best-fit Na D profile of 10 inflows. The marks are the same as Figure A1.

- Curtis-Lake, E., Cameron, A. J., Bunker, A. J., et al. 2025, arXiv e-prints, arXiv:2510.01033, doi: [10.48550/arXiv.2510.01033](https://doi.org/10.48550/arXiv.2510.01033)
- Davé, R., Finlator, K., & Oppenheimer, B. D. 2011, MNRAS, 416, 1354, doi: [10.1111/j.1365-2966.2011.19132.x](https://doi.org/10.1111/j.1365-2966.2011.19132.x)
- Davies, R. L., Belli, S., Park, M., et al. 2024, MNRAS, 528, 4976, doi: [10.1093/mnras/stae327](https://doi.org/10.1093/mnras/stae327)
- de Graaff, A., Brammer, G., Weibel, A., et al. 2025, A&A, 697, A189, doi: [10.1051/0004-6361/202452186](https://doi.org/10.1051/0004-6361/202452186)
- D'Eugenio, F., Pérez-González, P. G., Maiolino, R., et al. 2024a, Nature Astronomy, 8, 1443, doi: [10.1038/s41550-024-02345-1](https://doi.org/10.1038/s41550-024-02345-1)
- D'Eugenio, F., Pérez-González, P. G., Maiolino, R., et al. 2024b, Nature Astronomy, 8, 1443, doi: [10.1038/s41550-024-02345-1](https://doi.org/10.1038/s41550-024-02345-1)
- Diamond-Stanic, A. M., Rieke, G. H., & Rigby, J. R. 2009, ApJ, 698, 623, doi: [10.1088/0004-637X/698/1/623](https://doi.org/10.1088/0004-637X/698/1/623)
- Duras, F., Bongiorno, A., Ricci, F., et al. 2020, A&A, 636, A73, doi: [10.1051/0004-6361/201936817](https://doi.org/10.1051/0004-6361/201936817)
- Eisenstein, D. J., Johnson, B. D., Robertson, B., et al. 2023, arXiv e-prints, arXiv:2310.12340, doi: [10.48550/arXiv.2310.12340](https://doi.org/10.48550/arXiv.2310.12340)
- Eisenstein, D. J., Willott, C., Alberts, S., et al. 2026, ApJS, 283, 6, doi: [10.3847/1538-4365/ae3163](https://doi.org/10.3847/1538-4365/ae3163)
- Falcón-Barroso, J., Sánchez-Blázquez, P., Vazdekis, A., et al. 2011, A&A, 532, A95, doi: [10.1051/0004-6361/201116842](https://doi.org/10.1051/0004-6361/201116842)
- Ferruit, P., Jakobsen, P., Giardino, G., et al. 2022, A&A, 661, A81, doi: [10.1051/0004-6361/202142673](https://doi.org/10.1051/0004-6361/202142673)
- Fluetsch, A., Maiolino, R., Carniani, S., et al. 2021, MNRAS, 505, 5753, doi: [10.1093/mnras/stab1666](https://doi.org/10.1093/mnras/stab1666)
- Foreman-Mackey, D., Hogg, D. W., Lang, D., & Goodman, J. 2013, PASP, 125, 306, doi: [10.1086/670067](https://doi.org/10.1086/670067)
- Förster Schreiber, N. M., Übler, H., Davies, R. L., et al. 2019, ApJ, 875, 21, doi: [10.3847/1538-4357/ab0ca2](https://doi.org/10.3847/1538-4357/ab0ca2)
- Franx, M., van Dokkum, P. G., Förster Schreiber, N. M., et al. 2008, ApJ, 688, 770, doi: [10.1086/592431](https://doi.org/10.1086/592431)
- French, K. D., Yang, Y., Zabludoff, A., et al. 2015, ApJ, 801, 1, doi: [10.1088/0004-637X/801/1/1](https://doi.org/10.1088/0004-637X/801/1/1)
- Gardner, J. P., Mather, J. C., Clampin, M., et al. 2006, SSRv, 123, 485, doi: [10.1007/s11214-006-8315-7](https://doi.org/10.1007/s11214-006-8315-7)
- Genin, A., Shuntov, M., Brammer, G., et al. 2025, A&A, 699, A343, doi: [10.1051/0004-6361/202555504](https://doi.org/10.1051/0004-6361/202555504)
- González-Alfonso, E., Fischer, J., Spoon, H. W. W., et al. 2017, ApJ, 836, 11, doi: [10.3847/1538-4357/836/1/11](https://doi.org/10.3847/1538-4357/836/1/11)
- Heintz, K. E., Brammer, G. B., Watson, D., et al. 2025, A&A, 693, A60, doi: [10.1051/0004-6361/202450243](https://doi.org/10.1051/0004-6361/202450243)
- Hopkins, P. F., Hernquist, L., Cox, T. J., & Kereš, D. 2008, ApJS, 175, 356, doi: [10.1086/524362](https://doi.org/10.1086/524362)
- Hopkins, P. F., Kereš, D., Oñorbe, J., et al. 2014, MNRAS, 445, 581, doi: [10.1093/mnras/stu1738](https://doi.org/10.1093/mnras/stu1738)
- Jakobsen, P., Ferruit, P., Alves de Oliveira, C., et al. 2022, A&A, 661, A80, doi: [10.1051/0004-6361/202142663](https://doi.org/10.1051/0004-6361/202142663)
- Ji, Z., & Gialvalisco, M. 2023, ApJ, 943, 54, doi: [10.3847/1538-4357/aca807](https://doi.org/10.3847/1538-4357/aca807)
- Ji, Z., Williams, C. C., Tacchella, S., et al. 2024a, ApJ, 974, 135, doi: [10.3847/1538-4357/ad6e7f](https://doi.org/10.3847/1538-4357/ad6e7f)
- Ji, Z., Williams, C. C., Rieke, G. H., et al. 2024b, arXiv e-prints, arXiv:2409.17233, doi: [10.48550/arXiv.2409.17233](https://doi.org/10.48550/arXiv.2409.17233)
- Ji, Z., Williams, C. C., Behroozi, P., et al. 2026, arXiv e-prints, arXiv:2604.05022, doi: [10.48550/arXiv.2604.05022](https://doi.org/10.48550/arXiv.2604.05022)
- Johnson, B. D., Leja, J., Conroy, C., & Speagle, J. S. 2021, ApJS, 254, 22, doi: [10.3847/1538-4365/abef67](https://doi.org/10.3847/1538-4365/abef67)
- Johnson, B. D., Robertson, B. E., Eisenstein, D. J., et al. 2026, arXiv e-prints, arXiv:2601.15954, doi: [10.48550/arXiv.2601.15954](https://doi.org/10.48550/arXiv.2601.15954)

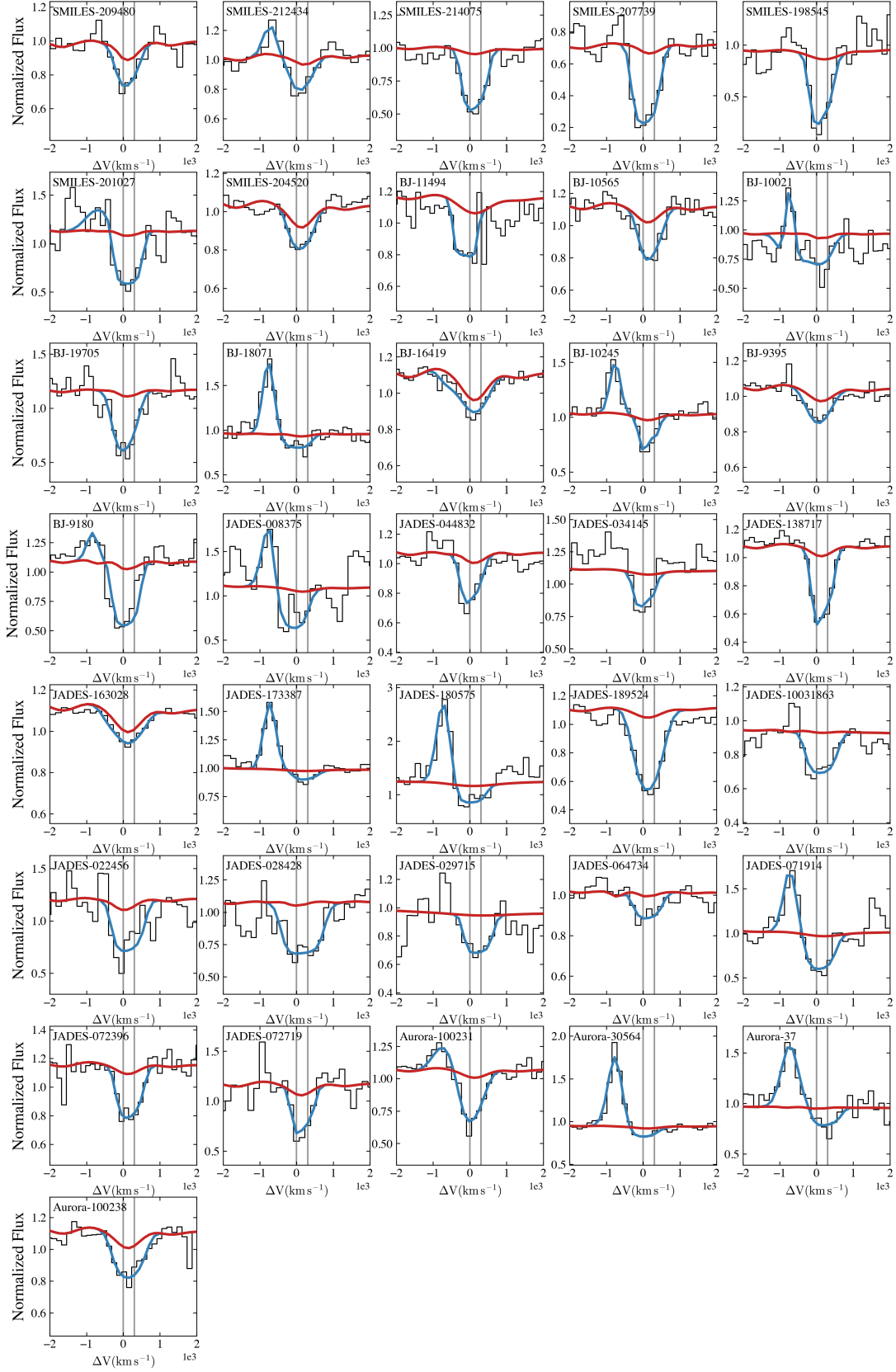


Figure A3. Best-fit Na D profile of 36 galaxies with Na D-traced systemic ISMs. The marks are the same as Figure A1.

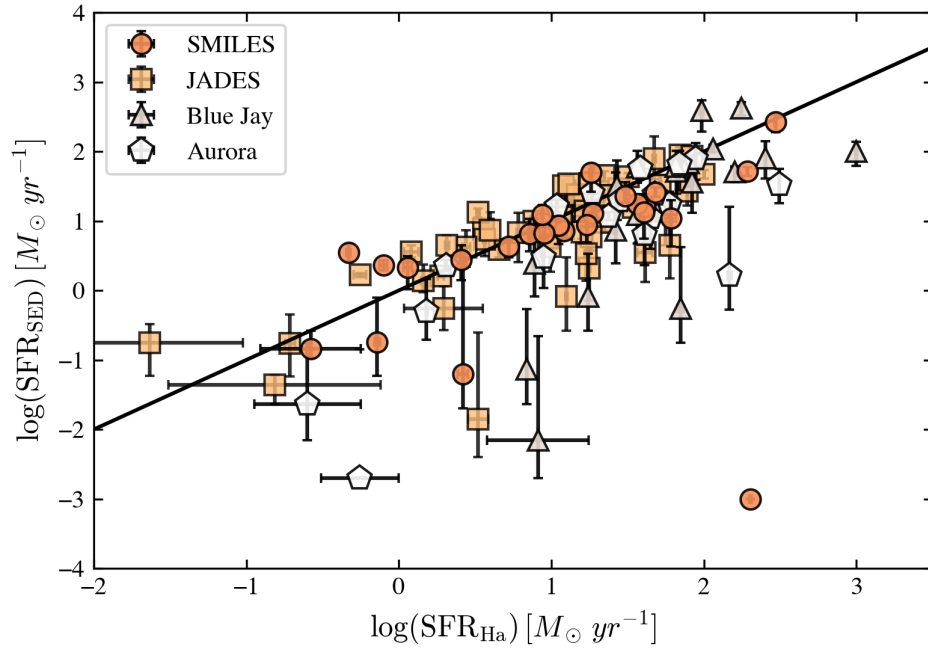


Figure B1. Comparison between H α -based SFR and SED-based SFR. Galaxies from the SMILES, JADES, Blue Jay, and Aurora surveys are marked by circles, squares, triangles, and pentagon, respectively. Overall the fiducial SFR from SED modeling agrees well with the H α measurements.

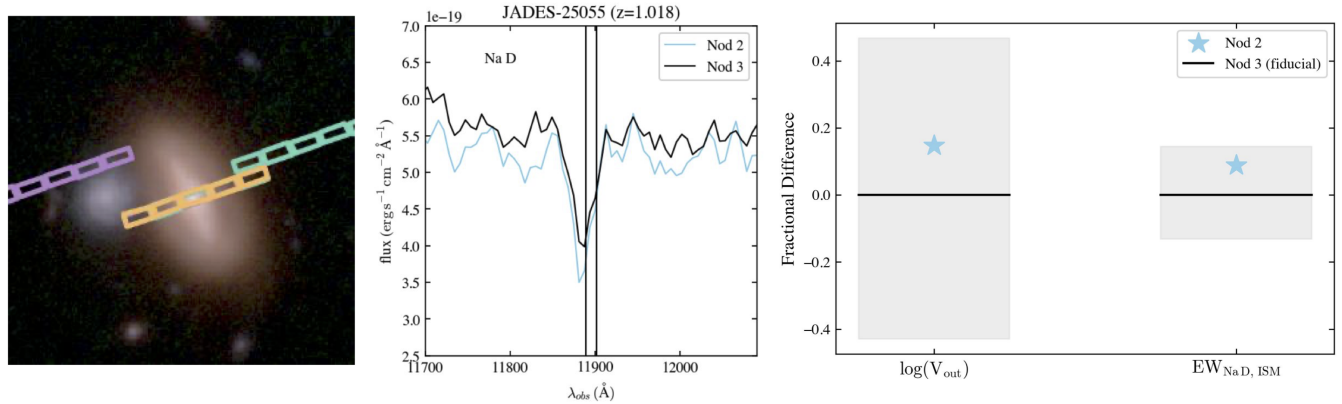


Figure C1. Comparison of spectra and Na D ISM profile measurements between 3-nod and 2-nod data reduction versions for JADES-25055 at $z=1.018$.

- Juodžbalis, I., Maiolino, R., Baker, W. M., et al. 2026, MNRAS, doi: [10.1093/mnras/stag086](https://doi.org/10.1093/mnras/stag086)
- Kauffmann, G., Heckman, T. M., Tremonti, C., et al. 2003, MNRAS, 346, 1055, doi: [10.1111/j.1365-2966.2003.07154.x](https://doi.org/10.1111/j.1365-2966.2003.07154.x)
- Kennicutt, R. C., & Evans, N. J. 2012, ARA&A, 50, 531, doi: [10.1146/annurev-astro-081811-125610](https://doi.org/10.1146/annurev-astro-081811-125610)
- Kereš, D., Katz, N., Fardal, M., Davé, R., & Weinberg, D. H. 2009, MNRAS, 395, 160, doi: [10.1111/j.1365-2966.2009.14541.x](https://doi.org/10.1111/j.1365-2966.2009.14541.x)
- Kewley, L. J., Dopita, M. A., Sutherland, R. S., Heisler, C. A., & Trevena, J. 2001, ApJ, 556, 121, doi: [10.1086/321545](https://doi.org/10.1086/321545)
- Kewley, L. J., Maier, C., Yabe, K., et al. 2013, ApJL, 774, L10, doi: [10.1088/2041-8205/774/1/L10](https://doi.org/10.1088/2041-8205/774/1/L10)
- King, A., & Pounds, K. 2015, ARA&A, 53, 115, doi: [10.1146/annurev-astro-082214-122316](https://doi.org/10.1146/annurev-astro-082214-122316)
- Kroupa, P. 2001, MNRAS, 322, 231, doi: [10.1046/j.1365-8711.2001.04022.x](https://doi.org/10.1046/j.1365-8711.2001.04022.x)
- Leitherer, C., Schaerer, D., Goldader, J. D., et al. 1999, ApJS, 123, 3, doi: [10.1086/313233](https://doi.org/10.1086/313233)
- Leja, J., Johnson, B. D., Conroy, C., van Dokkum, P. G., & Byler, N. 2017, ApJ, 837, 170, doi: [10.3847/1538-4357/aa5ffe](https://doi.org/10.3847/1538-4357/aa5ffe)
- Leja, J., Speagle, J. S., Ting, Y.-S., et al. 2022, ApJ, 936, 165, doi: [10.3847/1538-4357/ac887d](https://doi.org/10.3847/1538-4357/ac887d)
- Liu, D., Lang, P., Magnelli, B., et al. 2019, ApJS, 244, 40, doi: [10.3847/1538-4365/ab42da](https://doi.org/10.3847/1538-4365/ab42da)
- Luo, B., Brandt, W. N., Xue, Y. Q., et al. 2017, ApJS, 228, 2, doi: [10.3847/1538-4365/228/1/2](https://doi.org/10.3847/1538-4365/228/1/2)
- Luo, Y., Rowlands, K., Alatalo, K., et al. 2022, ApJ, 938, 63, doi: [10.3847/1538-4357/ac8b7d](https://doi.org/10.3847/1538-4357/ac8b7d)
- Lyu, J., Alberts, S., Rieke, G. H., & Rujopakarn, W. 2022, ApJ, 941, 191, doi: [10.3847/1538-4357/ac9e5d](https://doi.org/10.3847/1538-4357/ac9e5d)
- Lyu, J., Alberts, S., Rieke, G. H., et al. 2024, ApJ, 966, 229, doi: [10.3847/1538-4357/ad3643](https://doi.org/10.3847/1538-4357/ad3643)
- Madau, P. 1995, ApJ, 441, 18, doi: [10.1086/175332](https://doi.org/10.1086/175332)
- Madau, P., & Dickinson, M. 2014, ARA&A, 52, 415, doi: [10.1146/annurev-astro-081811-125615](https://doi.org/10.1146/annurev-astro-081811-125615)
- Man, A., & Belli, S. 2018, Nature Astronomy, 2, 695, doi: [10.1038/s41550-018-0558-1](https://doi.org/10.1038/s41550-018-0558-1)
- Muzzin, A., Marchesini, D., Stefanon, M., et al. 2013, ApJ, 777, 18, doi: [10.1088/0004-637X/777/1/18](https://doi.org/10.1088/0004-637X/777/1/18)
- Naab, T., & Ostriker, J. P. 2017, ARA&A, 55, 59, doi: [10.1146/annurev-astro-081913-040019](https://doi.org/10.1146/annurev-astro-081913-040019)
- Nenkova, M., Sirocky, M. M., Ivezić, Ž., & Elitzur, M. 2008a, ApJ, 685, 147, doi: [10.1086/590482](https://doi.org/10.1086/590482)
- Nenkova, M., Sirocky, M. M., Nikutta, R., Ivezić, Ž., & Elitzur, M. 2008b, ApJ, 685, 160, doi: [10.1086/590483](https://doi.org/10.1086/590483)
- Netzer, H. 2009, MNRAS, 399, 1907, doi: [10.1111/j.1365-2966.2009.15434.x](https://doi.org/10.1111/j.1365-2966.2009.15434.x)
- Netzer, H. 2019, MNRAS, 488, 5185, doi: [10.1093/mnras/stz2016](https://doi.org/10.1093/mnras/stz2016)
- Noeske, K. G., Weiner, B. J., Faber, S. M., et al. 2007, ApJL, 660, L43, doi: [10.1086/517926](https://doi.org/10.1086/517926)
- Noll, S., Burgarella, D., Giovannoli, E., et al. 2009, A&A, 507, 1793, doi: [10.1051/0004-6361/200912497](https://doi.org/10.1051/0004-6361/200912497)
- Park, M., Conroy, C., Johnson, B. D., et al. 2025, ApJ, 994, 165, doi: [10.3847/1538-4357/ae0cba](https://doi.org/10.3847/1538-4357/ae0cba)
- Park, M., Belli, S., Conroy, C., et al. 2024, ApJ, 976, 72, doi: [10.3847/1538-4357/ad7e15](https://doi.org/10.3847/1538-4357/ad7e15)
- Pennell, A., Runnoe, J. C., & Brotherton, M. S. 2017, MNRAS, 468, 1433, doi: [10.1093/mnras/stx556](https://doi.org/10.1093/mnras/stx556)
- Pérez-González, P. G., D'Eugenio, F., Rodríguez del Pino, B., et al. 2025, Nature Astronomy, 9, 1240, doi: [10.1038/s41550-025-02586-8](https://doi.org/10.1038/s41550-025-02586-8)
- Perna, M., Cresci, G., Brusa, M., et al. 2019, A&A, 623, A171, doi: [10.1051/0004-6361/201834193](https://doi.org/10.1051/0004-6361/201834193)
- Poznanski, D., Prochaska, J. X., & Bloom, J. S. 2012, MNRAS, 426, 1465, doi: [10.1111/j.1365-2966.2012.21796.x](https://doi.org/10.1111/j.1365-2966.2012.21796.x)
- Prochaska, J. X., Kasen, D., & Rubin, K. 2011, ApJ, 734, 24, doi: [10.1088/0004-637X/734/1/24](https://doi.org/10.1088/0004-637X/734/1/24)
- Rieke, G. H., Alberts, S., Shivaee, I., et al. 2024, ApJ, 975, 83, doi: [10.3847/1538-4357/ad6cd2](https://doi.org/10.3847/1538-4357/ad6cd2)
- Robertson, B. E., Johnson, B. D., Tacchella, S., et al. 2026, arXiv e-prints, arXiv:2601.15956, doi: [10.48550/arXiv.2601.15956](https://doi.org/10.48550/arXiv.2601.15956)
- Rupke, D. S., Veilleux, S., & Sanders, D. B. 2005a, ApJS, 160, 115, doi: [10.1086/432889](https://doi.org/10.1086/432889)
- Rupke, D. S., Veilleux, S., & Sanders, D. B. 2005b, ApJS, 160, 87, doi: [10.1086/432886](https://doi.org/10.1086/432886)
- Rupke, D. S., Veilleux, S., & Sanders, D. B. 2005c, ApJ, 632, 751, doi: [10.1086/444451](https://doi.org/10.1086/444451)
- Rupke, D. S. N. 2018, Galaxies, 6, 138, doi: [10.3390/galaxies6040138](https://doi.org/10.3390/galaxies6040138)
- Salpeter, E. E. 1955, ApJ, 121, 161, doi: [10.1086/145971](https://doi.org/10.1086/145971)
- Sánchez-Blázquez, P., Peletier, R. F., Jiménez-Vicente, J., et al. 2006, MNRAS, 371, 703, doi: [10.1111/j.1365-2966.2006.10699.x](https://doi.org/10.1111/j.1365-2966.2006.10699.x)
- Sarzi, M., Kaviraj, S., Nedelchev, B., et al. 2016, MNRAS, 456, L25, doi: [10.1093/mnrasl/slv165](https://doi.org/10.1093/mnrasl/slv165)
- Schawinski, K., Koss, M., Berney, S., & Sartori, L. F. 2015, MNRAS, 451, 2517, doi: [10.1093/mnras/stv1136](https://doi.org/10.1093/mnras/stv1136)
- Scholtz, J., Carniani, S., Parlanti, E., et al. 2025, arXiv e-prints, arXiv:2510.01034, doi: [10.48550/arXiv.2510.01034](https://doi.org/10.48550/arXiv.2510.01034)
- Scholtz, J., D'Eugenio, F., Maiolino, R., et al. 2026, Nature Astronomy, doi: [10.1038/s41550-025-02751-z](https://doi.org/10.1038/s41550-025-02751-z)

- Shapley, A. E., Sanders, R. L., Topping, M. W., et al. 2025, *ApJ*, 980, 242, doi: [10.3847/1538-4357/adad68](https://doi.org/10.3847/1538-4357/adad68)
- Siegel, J. C., Setton, D. J., Greene, J. E., et al. 2025, *ApJ*, 985, 125, doi: [10.3847/1538-4357/adc7b7](https://doi.org/10.3847/1538-4357/adc7b7)
- Silk, J., & Rees, M. J. 1998, *A&A*, 331, L1, doi: [10.48550/arXiv.astro-ph/9801013](https://doi.org/10.48550/arXiv.astro-ph/9801013)
- Somerville, R. S., Popping, G., & Trager, S. C. 2015, *MNRAS*, 453, 4337, doi: [10.1093/mnras/stv1877](https://doi.org/10.1093/mnras/stv1877)
- Speagle, J. S., Steinhardt, C. L., Capak, P. L., & Silverman, J. D. 2014, *ApJS*, 214, 15, doi: [10.1088/0067-0049/214/2/15](https://doi.org/10.1088/0067-0049/214/2/15)
- Spilker, J., Bezanson, R., Barišić, I., et al. 2018, *ApJ*, 860, 103, doi: [10.3847/1538-4357/aac438](https://doi.org/10.3847/1538-4357/aac438)
- Strateva, I., Ivezić, Ž., Knapp, G. R., et al. 2001, *AJ*, 122, 1861, doi: [10.1086/323301](https://doi.org/10.1086/323301)
- Sun, Y., Lee, G.-H., Zabludoff, A. I., et al. 2024, *MNRAS*, 528, 5783, doi: [10.1093/mnras/stae366](https://doi.org/10.1093/mnras/stae366)
- Sun, Y., Lyu, J., Rieke, G. H., et al. 2025, *ApJ*, 978, 98, doi: [10.3847/1538-4357/ad973b](https://doi.org/10.3847/1538-4357/ad973b)
- Sun, Y., Ji, Z., Rieke, G. H., et al. 2026, *ApJ*, 997, 140, doi: [10.3847/1538-4357/ae2c83](https://doi.org/10.3847/1538-4357/ae2c83)
- Tacchella, S., Dekel, A., Carollo, C. M., et al. 2016, *MNRAS*, 457, 2790, doi: [10.1093/mnras/stw131](https://doi.org/10.1093/mnras/stw131)
- Tacchella, S., Conroy, C., Faber, S. M., et al. 2022, *ApJ*, 926, 134, doi: [10.3847/1538-4357/ac449b](https://doi.org/10.3847/1538-4357/ac449b)
- Taylor, E., Maltby, D., Almaini, O., et al. 2024, *MNRAS*, 535, 1684, doi: [10.1093/mnras/stae2463](https://doi.org/10.1093/mnras/stae2463)
- Taylor, E., Carnall, A. C., Maltby, D., et al. 2026, arXiv e-prints, arXiv:2601.02269, doi: [10.48550/arXiv.2601.02269](https://doi.org/10.48550/arXiv.2601.02269)
- Tremonti, C. A., Moustakas, J., & Diamond-Stanic, A. M. 2007, *ApJL*, 663, L77, doi: [10.1086/520083](https://doi.org/10.1086/520083)
- Valentino, F., Heintz, K. E., Brammer, G., et al. 2025, *A&A*, 699, A358, doi: [10.1051/0004-6361/202553908](https://doi.org/10.1051/0004-6361/202553908)
- Veilleux, S., Cecil, G., & Bland-Hawthorn, J. 2005, *ARA&A*, 43, 769, doi: [10.1146/annurev.astro.43.072103.150610](https://doi.org/10.1146/annurev.astro.43.072103.150610)
- Veilleux, S., Maiolino, R., Bolatto, A. D., & Aalto, S. 2020, *A&A Rv*, 28, 2, doi: [10.1007/s00159-019-0121-9](https://doi.org/10.1007/s00159-019-0121-9)
- Veilleux, S., & Osterbrock, D. E. 1987, in *NASA Conference Publication*, Vol. 2466, NASA Conference Publication, ed. C. J. Lonsdale Persson, 737–740
- Virtanen, P., Gommers, R., Oliphant, T. E., et al. 2020, *Nature Methods*, 17, 261, doi: [10.1038/s41592-019-0686-2](https://doi.org/10.1038/s41592-019-0686-2)
- Williams, C. C., Spilker, J. S., Whitaker, K. E., et al. 2021, *ApJ*, 908, 54, doi: [10.3847/1538-4357/abcbf6](https://doi.org/10.3847/1538-4357/abcbf6)
- Woo, J.-H., Bae, H.-J., Son, D., & Karouzos, M. 2016, *ApJ*, 817, 108, doi: [10.3847/0004-637X/817/2/108](https://doi.org/10.3847/0004-637X/817/2/108)
- Worthey, G., & Ottaviani, D. L. 1997, *ApJS*, 111, 377, doi: [10.1086/313021](https://doi.org/10.1086/313021)
- Wu, P.-F. 2025, *ApJ*, 978, 131, doi: [10.3847/1538-4357/ad98ef](https://doi.org/10.3847/1538-4357/ad98ef)
- Xue, Y. Q., Luo, B., Brandt, W. N., et al. 2016, *ApJS*, 224, 15, doi: [10.3847/0067-0049/224/2/15](https://doi.org/10.3847/0067-0049/224/2/15)
- Zhu, P., Ito, K., Valentino, F., et al. 2026, arXiv e-prints, arXiv:2602.17767, doi: [10.48550/arXiv.2602.17767](https://doi.org/10.48550/arXiv.2602.17767)
- Zhu, Y., Rieke, M. J., Ji, Z., et al. 2025, *ApJ*, 986, 162, doi: [10.3847/1538-4357/add2f4](https://doi.org/10.3847/1538-4357/add2f4)
- Zhu, Y., Bonaventura, N., Sun, Y., et al. 2026, *ApJ*, 997, 301, doi: [10.3847/1538-4357/ae29b4](https://doi.org/10.3847/1538-4357/ae29b4)
- Zubovas, K., Bialopetravičius, J., & Kazlauskaitė, M. 2022, *MNRAS*, 515, 1705, doi: [10.1093/mnras/stac1887](https://doi.org/10.1093/mnras/stac1887)